J. Astrophys. Astr. (2023) 44:38
https://doi.org/10.1007/s12036-023-09914-2

SCIENTIFIC REVIEW

Exploring diffuse radio emission in galaxy clusters and groups with uGMRT and SKA

SURAJIT PAUL[1,13,*], RUTA KALE[2], ABHIRUP DATTA[3], ARITRA BASU[4], SHARANYA SUR[5], VIRAL PAREKH[6,7], PRATEEK GUPTA[1,5], SWARNA CHATTERJEE[3], SAMEER SALUNKHE[1,2], ASIF IQBAL[8], MAMTA PANDEY-POMMIER[9], RAMIJ RAJA[3,6], MAJIDUL RAHAMAN[3,10], SOMAK RAYCHAUDHURY[11,12], BIMAN B. NATH[13] and SUBHABRATA MAJUMDAR[14]

[1]Department of Physics, Savitribai Phule Pune University, Pune 411007, India.
[2]National Centre for Radio Astrophysics (NCRA), Tata Institute of Fundamental Research (TIFR), Pune 411007, India.
[3]Department of Astronomy, Astrophysics and Space Engineering, Indian Institute of Technology Indore, Simrol 453552, India.
[4]Thüringer Landessternwarte, Sternwarte 5, 07778 Tautenburg, Germany.
[5]Indian Institute of Astrophysics, II Block, Koramangala, Bengaluru 560034, India.
[6]Department of Physics and Electronics, Rhodes University, P.O. Box 94, Makhanda 6140, South Africa.
[7]National Radio Astronomy Observatory (NRAO), 1003 Lopezille Rd, Socorro, NM 87801, USA.
[8]AIM, CEA, CNRS, Université Paris-Saclay, Université Paris Diderot, Sorbonne Paris Cité 91191, Gif-sur-Yvette, France.
[9]Laboratoire Univers et Particules de Montpellier (LUPM)/CNRS, Université de Montpellier, CC 072—Place Eugène Bataillon, 34095 Montpellier Cedex 5, France.
[10]Institute of Astronomy and Department of Physics, National Tsing Hua University, No. 101, Section 2, Kuang-Fu Road, Hsinchu 30013, Taiwan.
[11]Inter-University Centre for Astronomy and Astrophysics, Ganeshkhind, Pune 411007, India.
[12]Ashoka University, Rajiv Gandhi Education City, Sonipat 131029, India.
[13]Raman Research Institute, Bengaluru 560080, India.
[14]Tata Institute of Fundamental Research, 1 Homi Bhabha Road, Colaba, Mumbai 400005, India.
*Corresponding author. E-mail: surajit@physics.unipune.ac.in

MS received 2 May 2022; accepted 2 November 2022

Abstract. Diffuse radio emission has been detected in a considerable number of galaxy clusters and groups, revealing the presence of pervasive cosmic magnetic fields, and of relativistic particles in the large scale structure of the Universe. Since the radio emission in galaxy systems is faint and its spectrum is steep, its observations are largely limited by the instrument sensitivity and frequency of observation, leading to a dearth of information, more so for lower-mass systems. The recent commissioning or upgrade of several large radio telescope arrays, particularly at the low frequency bands (<GHz) is, therefore, a significant step forward. The unprecedented sensitivity of these new instruments, aided by the development of advanced calibration and imaging techniques, have helped in achieving unparalleled image quality and revolutionised the study of cluster-scale radio emission. At the same time, the development of state-of-the-art numerical simulations and the availability of supercomputing facilities have paved the way for high-resolution numerical modelling of radio emission, and the structure of the cosmic magnetic fields, associated with large-scale structures in the Universe, leading to predictions matching the capabilities of observational facilities. In view of these rapidly-evolving developments in modeling and observations, in this review, we summarise the role of new telescope arrays and the development of advanced imaging techniques and discuss the range of detections of various

This article is part of the Special Issue on "Indian Participation in the SKA".

Published online: 27 April 2023

kinds of cluster radio sources, both in dedicated surveys as well as in numerous individual studies. We pay specific attention to the kinds of diffuse radio structures that have been able to reveal the underlying physics in recent observations. In particular, we discuss observations of large-scale sections of the cosmic web in the form of supercluster filaments, and studies of emission in low-mass systems, such as poor clusters and groups of galaxies, and of ultra-steep spectrum sources, the last two being notably aided by low-frequency observations and high sensitivity of the instruments being developed. We also discuss and review the current theoretical understanding of various diffuse radio sources in clusters and the associated magnetic field and polarisation in view of the current observations and simulations. As the statistics of detections improve along with our theoretical understanding, we update the source classification schemes based on the intrinsic properties of these sources. We conclude by summarising the role of the upgraded GMRT (uGMRT) and our expectations from the upcoming Square Kilometre Array (SKA) observatories.

Keywords. Physical data and processes—shock waves—turbulence—magnetic fields techniques: radioastronomy—galaxies: clusters: general galaxies: groups: general radio continuum: general.

1. Radio observations of galaxy clusters

Clusters of galaxies are massive ($\gtrsim 10^{14}\ M_{\odot}$) and large ($\sim$Mpc scale) systems residing at the top of the hierarchy of extragalactic gravitationally-bound structures in the Universe. They are usually found embedded at the cross-roads of the cosmic web (Springel *et al.* 2006; van de Weygaert & Bond 2008) and many are found non-relaxed, indicating that they are still in the process of formation (Molnar 2016). Various physical processes in the components of these systems make them luminous enough to be detected in astronomical observations at various wavelengths. Clusters are generally thermalised, their hot intra-cluster baryonic medium being prominent in X-ray emission (Sarazin 1986). A number of them are also detected as diffuse sources at radio wavelengths (for a review: van Weeren *et al.* 2019), confirming their non-thermal energy content.

These diffuse continuum radio sources in galaxy clusters are associated with the intra-cluster medium (ICM) and are usually not associated with any optical counterparts in the system. Typically, their extent is in the range of 100 kpc to a few Mpc with diverse morphologies. The emission usually has a power-law energy distribution with a steep spectral index[1] ($\alpha \sim 1.3$). These sources are generally faint at GHz frequencies ($\sim$0.1–1 μJy arcsec^{-2} at 1.4 GHz), and the steepness of the spectrum is largely due to the nature of the injection spectra (Stroe *et al.* 2014a). The evolution of the plasma associated with the radio emission is controlled largely by synchrotron and inverse Compton energy losses, and thus, as the plasma gets older, it results in further steepening of the radio spectrum (e.g., van Weeren *et al.* 2009).

The cluster radio sources have been traditionally classified as radio halos, relics and mini-halos, depending mainly on their shape, the process of origin and the location within the cluster (e.g., Enßlin *et al.* 1998; Giovannini *et al.* 1999; Feretti & Giovannini 2008; Feretti *et al.* 2012). An updated version appears in a review by van Weeren *et al.* (2019), where a new class has been added combining the revived AGN fossil plasma sources ('phoenix') and Gently re-energised tails (GReETs, de Gasperin *et al.* 2017a), with a discussion on the characteristic properties of these sources.

Since these sources are low in brightness and have a steep spectrum, their detection is limited by the instrument sensitivity and the sophistication of imaging techniques. Therefore, the study of diffuse radio emission from clusters got a huge fillip with the advent of highly sensitive telescopes as well as with the development of advanced calibration and imaging software and pipelines.

The review is organised as follows. The role of large telescopes is described in Section 1.1 and the current software packages and methods are described in Section 1.2. We further summarise the large surveys conducted so far and their future scope in Section 2. The observational status of various kinds of cluster diffuse radio sources and the detection of associated magnetic fields have been updated in Section 3. Recently, systematic studies of the detection of diffuse radio sources from structures, apart from and beyond the clusters (such as super-cluster filaments, galaxy groups and poor clusters) have gained momentum. We summarise and update on these efforts in Section 4 and Section 5. Updates on the theoretical understanding of diffuse synchrotron radio emission, the role of AGN feedback and the origin and evolution of cosmic magnetic fields from various cluster sources along with the efforts made so far on numerical simulations on this matter have been

[1]The spectral index, α is defined as $S_\nu \propto \nu^{-\alpha}$, where S_ν is flux density at frequency ν.

presented in Section 6. With a better understanding of the origin of these radio sources, we propose a novel classification in Section 7. The role of uGMRT and the expectations from the upcoming SKA telescopes in the context of clusters have been summarised in Section 8, and conclusions outlined in Section 9.

1.1 *Role of large telescope arrays*

The first large diffuse radio source was discovered in the nearby Coma cluster (Large *et al.* 1959) with a size of 1.1 Mpc. Yet, to gather a sizeable sample of galaxy cluster scale diffuse radio emissions, it took more than five decades, mostly through targeted individual objects and a handful of dedicated surveys (Venturi *et al.* 2007, 2008, 2013; Giacintucci *et al.* 2011; Kale *et al.* 2013, 2015a; Parekh *et al.* 2017b; Paul *et al.* 2019).

In recent times, however, there has been a race for searching diffuse radio emission in clusters, especially from large surveys. A large sample of 115 clusters, though many among them are previously known, were observed under MeerKAT Galaxy Cluster Legacy Survey (MGCLS). MeerKAT has allowed us to study them at an unprecedented depth of 3 μJy beam^{-1} at wide L-band (900–1670 MHz) with full polarisation information (Knowles *et al.* 2022), revealing many new unique features of diffuse structures. LoFAR Two Meter Sky Survey (LoTSS-1 and 2), on the other hand, has given an opportunity to study the sky at low frequencies (central frequency of 144 MHz) with a median rms as low as 83 μJy beam^{-1} (Shimwell *et al.* 2019, 2022). For deep fields, maps are further deeper at 30 μJy beam^{-1} (Osinga *et al.* 2021). LoFAR has so far discovered more than ∼60 new clusters with halo, relics or revived fossil plasma sources (or candidates) (Mandal *et al.* 2020; Osinga *et al.* 2021; van Weeren *et al.* 2021; Botteon *et al.* 2022). Botteon *et al.* (2020b) and Hoang *et al.* (2019) even discovered ultra-steep spectrum and extremely faint radio bridges between the pairs of interacting clusters. Studies with LoFAR helped in mapping diffuse radio emissions from the supercluster members (Ghirardini *et al.* 2021) as well as constraining magnetic field in the filaments (Locatelli *et al.* 2021). Strikingly, ultra-steep spectrum halos have been discovered in massive relaxed clusters (Savini *et al.* 2019). The ultra-sensitive wideband frequency coverage by uGMRT made possible the study of extremely steep ($\alpha > 2.0$ and curved spectrum relic/phoenix emissions (Kale *et al.* 2018; Lal 2020). Low-mass clusters and groups that remained undetected due to their expected low luminosity have now been detected using the wideband uGMRT studies (Paul *et al.* 2021) as well as in LoFAR, the emission from the intra-group medium (Nikiel-Wroczyński *et al.* 2019). Spectral index studies of distant radio halos are done by combining data from uGMRT and LoFAR, two extremely sensitive telescopes working at complementary frequencies (Di Gennaro *et al.* 2021a).

1.2 *Role of imaging packages and pipelines*

A vital aspect of radio interferometry is processing the raw data from telescope observation and converting it to science-ready images. Owing to the low surface brightness of the cluster diffuse radio sources, dynamic range and sensitivity limitations at low frequencies makes them challenging targets. New generation radio interferometry comes with wideband wide-field observations, which have helped to scan the sky over a large field-of-view with improved sensitivity. Due to the large bandwidth, the observing radio frequency bands are also often crowded with several undesirable radio frequency interference (RFI), which should be removed properly for an improved image. AOFlagger (Offringa *et al.* 2010, 2012) is an automated pipeline for effective RFI excision with a faster execution time. Moreover, the resolution, sensitivity to extended emission and primary beam changes over the large bandwidth need to be accounted for wideband observations. Wide-field imaging suffers non-coplanar baseline aberration, which results in degradation of image and phase error and thus needs to be corrected for the w-term. The introduction of wide-field, multi-scale (MS) and multi-term (MT) multi-frequency synthesis (MFS) imaging (Rau & Cornwell 2011) helped to alleviate issues with wideband imaging and construct better spatial and spectral structure across a large field-of-view. The astronomical image processing system (AIPS), developed by National Radio Astronomy Observatory (NRAO), is one of the oldest imaging packages. While Common Astronomy Software Application (CASA: McMullin *et al.* 2007), developed by NRAO in the last decade, is more user-friendly. With flagging, direction-independent calibration, imaging techniques and post-deconvolution primary beam correction, CASA has been successful in providing science-ready images. The imaging algorithm of CASA includes MS-MFS and MT-MFS techniques, as well as the W-projection method (Cornwell *et al.* 2008) for correcting the effects from non-coplanar baselines. The joint channel deconvolution in WSClean imager (Offringa *et al.* 2014; Offringa & Smirnov 2017) with W-stacking algorithm performs imaging 2–3 orders

faster than CASA MS-MFS. In addition to these, radio interferometric observations are hampered by a variety of time-dependent instrumental and ionospheric effects, particularly, at low-frequency observations, and require direction-dependent calibration methods. These effects are well represented by Jones matrices and are now being addressed, thanks to upgraded calibration techniques. Source peeling and atmosphere modelling (SPAM: Intema *et al.* 2009, 2017) is a widely used pipeline for both direction-independent and -dependent calibration for GMRT. KillMS (Tasse 2014) and DD-Facet (Tasse *et al.* 2018), Facet-based imaging software, are exceptional in dealing with externally defined direction-dependent Jones matrices and varying beam patterns for LoFAR. KillMS, DD-Facet can also be used for other telescopes like GMRT, VLA, MeerKAT and ATCA. With the A-projection algorithm (Bhatnagar *et al.* 2008), the pointing errors and errors induced due to asymmetric antenna power pattern can be removed during deconvolution.

Larger arrays increase the data size, escalating the computing load for imaging and calibration. Manual data reduction for these big data sets is both labour-intensive and error-prone, and thus, requires modern processing pipelines. With the introduction of automated and semi-automated pipelines, for instance, VLA calibration pipeline for updated VLA data, SPAM and CAPTURE for GMRT (Kale & Ishwara-Chandra 2021), Apercal for WSRT data reduction (Schulz *et al.* 2020), CARACal (Józsa *et al.* 2020) for MeerKAT, data handling has been made easier. The WSClean+IDG algorithm applies the correction in the image plane instead of the visibility plane and maps large sky areas with better efficiency and less computational cost (Sweijen *et al.* 2022). CubiCal (Kenyon *et al.* 2018) is a cython-based calibration package designed for multiprocessing and much faster execution. Recent studies by Wilber *et al.* (2020) and Parekh *et al.* (2021) have shown how the use of these software packages has significantly improved image dynamic range.

These highly sensitive telescopes and the development of advanced and sophisticated imaging packages and pipelines have helped in revealing a number of sources with new and unclassifiable properties, especially, plenty of ultra-steep and curved spectrum sources. Also, the discovery of many low-mass clusters with diffuse radio sources, with widely differing values of radio power, exceeded theoretical expectations. Interestingly, though it took six decades of radio observations to discover about 200 diffuse radio sources associated with galaxy clusters, only the last three years of observations have revealed more than 100 new sources (Botteon *et al.* 2022) with these new instruments, even from a limited sky coverage. LoFAR, from the Planck clusters list alone, is predicted to discover roughly 350 new clusters (Botteon *et al.* 2022) with diffuse radio sources in the near future, from the entire northern sky.

1.3 *uGMRT and SKA*

GMRT is a radio telescope array located in Khodad, near Pune, India (Swarup *et al.* 1991). It consists of 30 dish antennas with a diameter of 45 m each, spread in a roughly 'Y'-shaped array forming baselines with lengths in the range of 100 m–25 km. Upgrade of the GMRT involved the replacement of the earlier narrowband receivers with broadband ones and a new correlator (GMRT wideband backend) that allows recording data with instantaneous bandwidths of up to 400 MHz (Gupta *et al.* 2017). The wideband observations (400 MHz) as compared to the earlier narrowband ones (33 MHz) imply an improvement in sensitivity by a factor of 3.4. Most importantly, in the context of imaging diffuse radio sources, it significantly improves the UV-coverage. A simulation study of imaging extended sources with the uGMRT shows that there will be considerable improvement in recovering the morphology of extended sources due to the improved UV-coverage (Deo & Kale 2017).

The SKA is proposed to be the largest radio observatory to be built. Phase 1 will consist of two parts: SKA1-mid and SKA1-low. The SKA1-mid will operate in the frequency range of 350 MHz–15 GHz and will consist of 197 dish antennas offering maximum baseline lengths of up to 150 km. The SKA1-low will operate at 50–350 MHz and will be an aperture array of 512 stations spread over an array offering maximum baselines of 65 km (Braun *et al.* 2019). The SKA will be able to image the sky south of declination +44°.

In the context of diffuse radio emission from galaxy clusters, the SKA 1 is expected to uncover radio halo emission in thousands of clusters up to the redshift of 0.6 (Cassano *et al.* 2015; Kale *et al.* 2016) and similarly for mini-halos (Gitti *et al.* 2018), allowing to compare the status of magnetic fields in low and high redshift clusters. With SKA pathfinders, such as the uGMRT and precursor facilities, we expect to get a glimpse of the possible science.

2. Radio surveys of galaxy clusters

The search for diffuse emission in galaxy clusters has been carried out systematically by either using all-sky radio surveys or targeted observations. The GMRT Radio Halo Survey (GRHS) carried out at 610 MHz was the first, large and targeted sub-GHz survey of galaxy clusters (Venturi *et al.* 2007, 2008). The GRHS and its extension, together referred as the EGRHS, consisted of 64 clusters selected from the REFLEX and eBCS catalogues with the criteria: X-ray luminosity $>5 \times 10^{44}$ erg s^{-1}, redshift in the range of 0.2–0.4 and declination $>-30°$ (Kale *et al.* 2013, 2015b). The occurrence of radio halos was found in 22%, of relics in 5%, and of mini-halos in 16% of the EGRHS sample. A total of 31 upper limits for radio halos and five for mini-halos were reported using the method of injection of model radio halos in the cases of non-detections (Kale *et al.* 2013, 2015b). Further to this survey, with the availability of Sunyaev–Zel'dovich (SZ)-detected clusters, nearly complete mass-limited samples have been surveyed. A scaling relation between the radio halo power and the integrated SZ effect measurements (host cluster mass) and the weakness of the bimodality in this plane was reported by Basu (2012). Targeted studies of Planck-discovered clusters also revealed new radio halos (e.g., Bagchi *et al.* 2011; Bonafede *et al.* 2015). Further, Cuciti *et al.* (2021a) have surveyed 75 galaxy clusters from the Planck catalogue in the redshift range of 0.08–0.33 with masses and $M_{500} > 6 \times 10^{14}\ M_{\odot}$. In this study, it was found that ∼90% of the radio halos are hosted in merging clusters, and their radio power is correlated with the mass of the host clusters, albeit with a large dispersion. Surveys of samples selected from the Massive Cluster Survey (MACS) and the South Pole Telescope have also revealed new cluster radio sources (Parekh *et al.* 2017b; Paul *et al.* 2019; Raja *et al.* 2021).

MeerKAT, the precursor for the SKA in South Africa, has recently released the radio images of about 115 clusters at 1280 MHz, called the MeerKAT Galaxy Cluster Legacy Survey (MGCLS; Knowles *et al.* 2022). This sample spans a declination range of −85 to 0°, a redshift range of $0.011 < z < 0.87$ and consists of X-ray and radio-selected clusters based on published works and the MCXC catalogue. The first glimpse at samples of clusters at high redshifts (>0.5) was recently possible with the LOFAR. Among 20 clusters that were sampled, radio halos were found in ∼50% of the clusters, which imply that a process of fast magnetic amplification may be playing a role (Di Gennaro *et al.* 2021b). The largest survey so far has been done recently by Botteon *et al.* (2022), taking a list of 309 clusters from the second catalogue of Planck SZ-detected sources that were in the area of 5634 deg^2 covered by the Second Data Release of the LOFAR Two-meter Sky Survey (LoTSS-DR2). The survey has median redshift of $z = 0.280$ in the range of $0.016 < z < 0.9$ and mass range of $1.1 \times 10^{14}\ M_{\odot} < M_{500} < 11.7 \times 10^{14}\ M_{\odot}$. With a median rms noise of 83 μJy, out of 309 clusters, 83 clusters are found to host radio halos, including candidate halos and 26 are detected with radio relics and candidate relics, with an overall detection rate of 30 ± 11% halos and 10 ± 6% relics, of which almost 50% are new detection. This survey also includes the earlier survey of HETDEX spring region using LOFAR telescope (van Weeren *et al.* 2021). We show the large surveys of clusters in the sky in Figure 1.

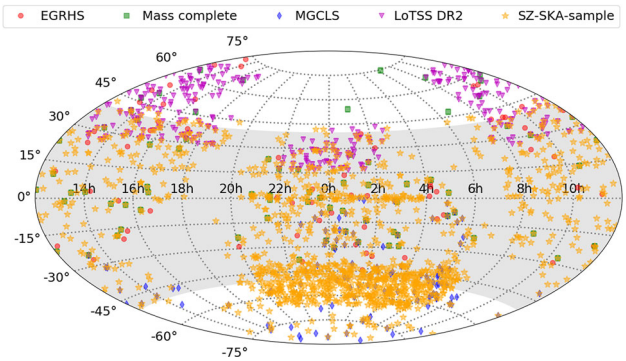

Figure 1. Various samples of galaxy clusters surveyed in the last decade are shown in an Aitoff projection of the sky. The red circles show the clusters in the Extended GMRT Radio Halo Survey (Kale *et al.* 2015b), the green squares show the mass complete extension of EGRHS (Cuciti *et al.* 2021a), the blue diamonds show the MeerKAT Galaxy Cluster Legacy Survey (Knowles *et al.* 2022) and magenta triangles show the Planck clusters surveyed in LoTSS DR2 (Botteon *et al.* 2022). The SKA will enable radio surveys of a large sample of galaxy clusters in the southern sky, such as the SZ-detected clusters from Planck Collaboration *et al.* (2017) shown by stars. The sky that is accessible to both uGMRT and the SKA is shown in grey.

Targeted radio surveys with interferometers such as GMRT requires long observations and thus, if suitable surveys of wide regions of the sky are available, the search for diffuse emission in galaxy clusters can speed up considerably. In Figure 1, we have marked the cluster sample from the Planck, which will be accessible for studies with the SKA. There is a large overlap in the cluster samples accessible to uGMRT and the SKA between the declinations of −50° and +40°.[2]

[2]Limiting declination is taken to be the one where the observing time is 3.5 h given the elevation limit of the respective telescope.

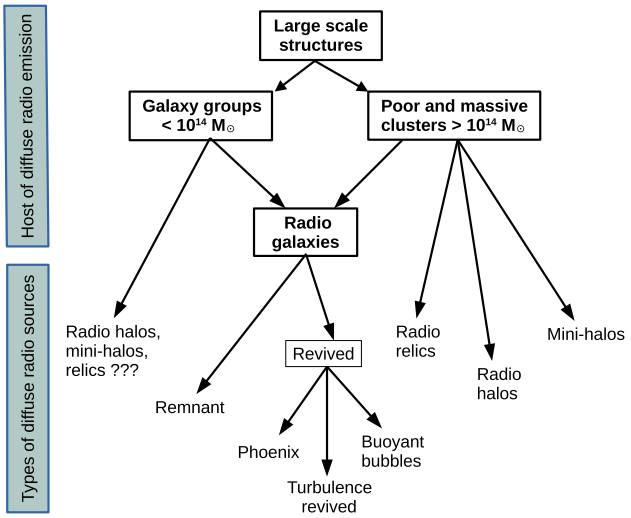

Figure 2. Schematic diagram for the classification of cluster diffuse radio sources.

3. Diffuse radio sources in clusters

3.1 *Current classification of cluster radio sources*

With the growing statistics of the diffuse cluster radio sources, to ease systematic studies, one needs classifying these sources. Historically, these sources were classified broadly into radio halos, relics and mini-halos, based on a mixture of their location and the origin (Enßlin *et al.* 1998; Giovannini *et al.* 1999; Feretti & Giovannini 2008; Feretti *et al.* 2012). Recently, with ample of data availability and with a better understanding of these sources, van Weeren *et al.* (2019) have made a new classification where they clubbed radio halo and mini-halos under the name (i) radio-halo, depending on their location and shape. Instead of radio relics, they named them (ii) cluster radio shocks, depending on their mechanism of origin, and finally, defined a new class of objects as (iii) revived active galactic nuclei (AGN) fossil plasma sources, phoenices, and GReET, because of their ultra-steep spectrum nature. Depending on the current classification schemes, we provide here a schematic diagram in Figure 2, and present the updates on these various diffuse radio sources in further subsections.

Although, radio halos, mini-halos and cluster radio shocks in general, show a power-law spectrum, AGN relics or fossil plasma sources and phoenices show a rather curved spectrum due to the ageing effect. While the power-law spectrum favours an *in-situ* particle acceleration mechanism, spectral curvature indicates the dying or revival of aged synchrotron emitting electrons (van Weeren *et al.* 2019). It shows that the distinct nature of these sources depends primarily on the initial spectrum of the electrons and the dynamics of the ICM. With the large number of discoveries of diffuse radio sources in and around galaxy clusters, a reconsideration of the classification may be needed.

3.2 *Radio halos and mini-halos*

Diffuse and mega-parsec-sized radio sources that extend over the cluster volume, are more or less co-spatial with the thermal X-ray emitting gas of the ICM and cannot be associated with any of the cluster galaxies, are termed as radio halos. Radio halos typically have radio powers at 1.4 GHz in the range of 10^{23}–10^{26} W Hz^{-1} and are found to be unpolarised (Feretti & Giovannini 2008; Giovannini *et al.* 2009). The most powerful radio halos have been found in merging clusters (e.g., Buote 2001; Cassano *et al.* 2010). The radio halos are proposed to be powered by a re-acceleration process involving turbulence (Brunetti & Jones 2014, for review) and the underlying population of relativistic electrons that are produced as a by-product of the hadronic collisions (Dennison 1980; Schlickeiser *et al.* 1987). Part of the mildly relativistic seed electron population may also be a result of the radio galaxies in the cluster. The theoretical models in this regard are described in Section 6.

Radio mini-halos are diffuse radio sources surrounding the brightest cluster galaxies (BCGs) in relaxed, cool-core clusters, and have extents ∼100–500 kpc. Otherwise, they have observational radio properties almost similar to that of radio halos. Mini-halos are known to occur in both low and high redshift clusters, such as redshift 0.018 (Perseus cluster, Sijbring 1993) and redshift 0.596 (Phoenixcluster, van Weeren *et al.* 2014; Raja *et al.* 2020b). A mini-halo has been recently reported in the cluster ACT-CL J0022.20036 at redshift 0.8050 (Knowles *et al.* 2019) and an intermediate radio halo in SPT-CL J2031−4037 (Raja *et al.* 2020a). The spectral indices (α) of the few mini-halos that are known, are in the range of 1.2–1.6 at frequencies between 300 and 1400 MHz (Giacintucci *et al.* 2014; Richard-Laferrière *et al.* 2020). The correlation between the BCG and MH radio luminosities indicates that the radio emission from the BCG itself (known to be AGN feedback due to multiphase cooling of cluster cores) may have a crucial role to play (Giacintucci *et al.* 2014). In a recent work, Richard-Laferrière *et al.* (2020) have studied a sample of 33 clusters with mini-halos and explored the connection between the BCG and the mini-halo. They suggest a connection

between the feedback processes at the AGN and mini-halo, in line with the earlier hypothesis by Bravi *et al.* (2016).

The X-ray properties of clusters hosting mini-halos and radio halos are found to be very different. Mini-halos are found in relaxed clusters and radio halos in merging clusters (e.g., Cassano *et al.* 2010; Kale *et al.* 2015b). The distribution of central entropy (K_0) in galaxy clusters shows that the clusters hosting mini-halos have $K_0 < 20$ keV cm^2 and those hosting radio halos typically have $K_0 > 50$ keV cm^2 (Giacintucci *et al.* 2017).

The division between mini-halos and radio halos is getting blurred due to deeper observations leading to new discoveries that challenge the current classification. Theoretical models have also proposed that the clusters that are intermediate to merging or relaxed may show the presence of diffuse sources with properties consistent with mini-halos as well as radio halos (Brunetti & Jones 2014). There are examples of transition systems such as RXCJ0232.2-4420 (Kale *et al.* 2019) and also mini-halos that have a more extended component (Sommer & Basu 2014; Venturi *et al.* 2017) which is also steeper in spectrum (e.g., Savini *et al.* 2018, 2019; Rahaman *et al.* 2021). Classification as a mini-halo or a radio halo requires availability of X-ray data. In the recent search for diffuse radio emission in the LoFAR DR2 (Shimwell *et al.* 2022), the term mini-halo has been dropped to avoid the uncertain classification until X-ray data become available, and the term radio halo is used to describe centrally located diffuse radio emission in clusters (Botteon *et al.* 2022). A new look at the classification may be needed, in view of the variety of sources that are discovered.

3.3 *Radio relics (cluster radio shocks)*

Radio relics or cluster radio shocks are diffuse radio sources with elongated or arc-like morphology that typically occur at the peripheries of clusters, usually coinciding with the X-ray shocks. In some cases a pair of such sources occur on nearly opposite peripheries of clusters and these are termed as double radio relics (Bonafede *et al.* 2017). These radio shocks are found with sizes up to several Mpc, comparatively flatter spectrum than radio halos/mini-halos and are highly polarised having fractional polarisation $p \sim$ 10–50% at 1.4 GHz; (van Weeren *et al.* 2009; Kierdorf *et al.* 2017; de Gasperin *et al.* 2022; Rajpurohit *et al.* 2022; Schellenberger *et al.* 2022).

Relics were proposed as originating in accretion shocks at cluster outskirts (e.g., Enßlin *et al.* 1998). However, evidence from morphologies and spectral indices suggests that the shocks are most likely merger shocks that travel outward with respect to the cluster centre (Paul *et al.* 2011; Nuza *et al.* 2017). The Mach numbers of the underlying shocks are in the range of 1–4, which are much lower than expected for accretion shocks (Markevitch & Vikhlinin 2007). Observational evidence has been found in a few clusters showing an overall consistency of radio and X-ray derived Mach numbers (Akamatsu & Kawahara 2013; Rajpurohit *et al.* 2021a; Chatterjee *et al.* 2022) supporting the merger shock scenario. Moreover, the polarisation studies also exhibit aligned magnetic fields, along with the elongation of the relics (e.g., van Weeren *et al.* 2010; Kale *et al.* 2012; Rajpurohit *et al.* 2021a).

3.4 *Remnant radio galaxies*

After the jets of radio galaxies cease to be active, the radio lobes evolve passively unless disturbed by any other event in the surrounding medium. Due to synchrotron radiation and inverse-Compton scattering, the relativistic electrons lose energy rapidly, making the radio lobe fainter. Over time scales of a million years or so, the lobe can be undetectable. Such diffuse radio sources can be found in clusters. The pressure of the intra-cluster medium can lead to confinement of the lobes and prevent expansion losses (Enßlin & Gopal-Krishna 2001). Steep spectrum diffuse radio sources, which have morphologies like double lobes, but no obvious jet and a core can be classified as remnant radio galaxies (e.g., Murgia *et al.* 2011; Salunkhe *et al.* 2022). A sample of such sources having steep spectra extracted from the NVSS and VLSS surveys was presented by Dwarakanath & Kale (2009). Also, more recent studies with the Murchison Wide-field Array as well as MeerKAT (MGCLS) have resulted in discoveries of remnant radio galaxies (Hodgson *et al.* 2021; Oozeer *et al.* 2021; Quici *et al.* 2021; Knowles *et al.* 2022). However, such sources need not necessarily have steep spectra, as can be seen based on the properties of the remnant discovered with the LOFAR (Brienza *et al.* 2016). Deeper surveys are likely to expand the samples of such remnants as we reach fainter levels of detection across the frequency range, such as covered by the SKA precursors and pathfinders. Systematic search in these images can result in a census of such sources

that will throw light on the late stages of radio lobe evolution.

3.5 *Revived cluster diffuse radio sources*

Numerous examples of another class of sources have been discovered with the availability of highly sensitive low-frequency radio telescopes such as LoFAR and uGMRT, in recent times. They are of ultra-steep spectrum ($\alpha < -1.5$), mostly with high spectral age with curved spectrum at high frequencies and are found anywhere inside the clusters (see Figure 3). Usually, they are known as phoenices or AGN relics (van Weeren *et al.* 2019). As the classification suggests, this diffuse emission comes from the revival or re-energisation of fossil non-thermal electrons in clusters due to the passage of a shock or turbulence. The hosts of these sources are often the jets present in the cluster associated with AGN, in their radio-inactive phase. The spectral age of these jets or lobes are tens of Myr (Enßlin & Gopal-Krishna 2001). The faded synchrotron emission (see Section 3.4) from these sources are boosted by shock compression or gentle re-energisation or complex plasma interaction and appear bright in sub-GHz radio band (Enßlin & Gopal-Krishna 2001; de Gasperin *et al.* 2017a). These sources typically have ultra-steep integrated spectrum with $\alpha < -1.5$ (Mandal *et al.* 2019), shows steepening and curvature at high frequencies (Slee *et al.* 2001) and irregular spectral index distribution (Mandal *et al.* 2020). They do not have specific location or shape-based classification. The ultra steep nature makes them difficult to detect at GHz frequency, and thus, these sources remain unexplored in detail. Though the low spatial resolution of the low-frequency sky surveys like TGSS, GLEAM, VLSS, etc., makes it challenging to distinguish these sources from other diffuse structures, with the improvement of telescope facilities in recent times, several fossil sources have been discovered (de Gasperin *et al.* 2017a; Mandal *et al.* 2019, 2020; Duchesne *et al.* 2021, 2022; Brienza *et al.* 2022). Recent discoveries have helped in quantifying properties of these revived plasma sources and have significantly improved our understanding.

3.5.1 Radio phoenix Although most of the diffuse radio sources from the peripheral regions of clusters have been traditionally classified as radio relics, some of these sources clearly have different physical origins, which led (e.g., Kempner *et al.* 2004) to suggest a different scheming of naming them based on our understanding of their origin. The radio phoenix is a class of diffuse source (e.g., Enßlin & Gopal-Krishna 2001), where a plasma bubble resulting from past AGN activity is compressed by a passing shock wave (possibly from a recent merger). This provides sufficient energy to re-energize the relativistic electrons and also enhances the magnetic field strength. This results into a low power steep-spectrum radio source, now classified as radio phoenix. Simulations (e.g., Enßlin & Brüggen 2002) have been used to find likely candidates in radio observations. These sources can be both roundish (e.g., Abell 1664, Kale & Dwarakanath 2012), or elongated (e.g., Abell 2048, van Weeren *et al.* 2009; A3017, Pandge *et al.* 2021), both in rich clusters (e.g., Abell 85, Knowles *et al.* 2022; Rahaman *et al.* 2022) or poorer systems (e.g., IC1262, Pandge *et al.* 2019), and can be found in a range of cluster-centric radius, but closer to the core than in the case of the radio relics. Furthermore, unlike relics, radio phoenices are found in both merging and relaxed clusters.

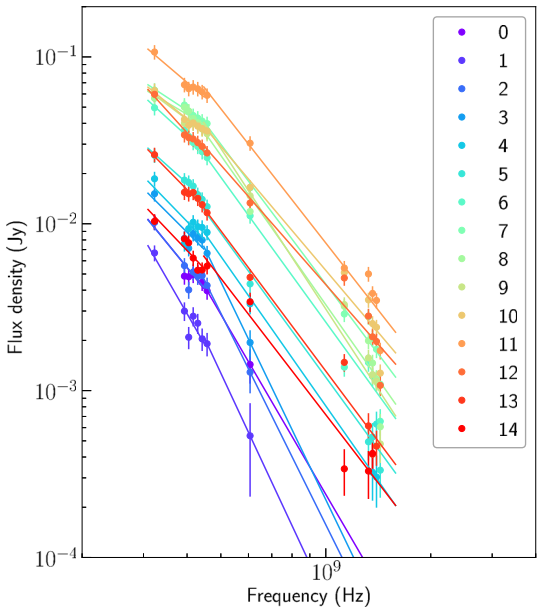

Figure 3. Curved spectra of A4038 phoenix for different regions of the phoenix marked in different colours as mentioned in Kale *et al.* (2018).

3.5.2 Turbulence-revived ultra-steep spectrum sources Turbulence, as well as a passing shock wave, can revive old fossil plasma in the ICM. The first case of this kind was observed in the cluster of galaxies Abell 1033 (de Gasperin *et al.* 2017a), where the tail of a WAT source gradually fades and then suddenly starts to brighten again. A spectral study of this source also shows the flattening of the spectrum in this part of the tail. A possible mechanism behind this source was proposed to be second-order Fermi acceleration by the turbulence

generated by Rayleigh–Taylor and Kelvin–Helmholtz instabilities in the tail. Two other similar sources are found in ZwCl 0634.1+4750 (Cuciti *et al.* 2018) and Abell 1314 (Wilber *et al.* 2019). Because of very few known examples of these sources, very little is understood about them. Future large scale surveys may provide to work with a decent sample.

3.5.3 Buoyant radio bubbles The X-ray image of a handful of cool-core clusters has shown cavities near the central BCG, often coincident with buoyantly rising radio bubbles from the central AGN (Fabian *et al.* 2000; McNamara *et al.* 2000; Clarke *et al.* 2005; Su *et al.* 2017). These buoyant radio bubbles interact with the ICM, inducing subsonic turbulence and offsetting the overall cooling of the gas. So far, no evidence of strong shock has been found near these bubbles (Churazov *et al.* 2013). Simulations have shown that the rise of the bubbles in the ICM undergoes Rayleigh–Taylor (RT) and Kelvin–Helmholtz (KH) instabilities, and their expansion is closely comparable to the mushroom clouds formed by massive explosions on the Earth (Saxton *et al.* 2001; Reynolds *et al.* 2005; Gardini 2007). The instabilities are balanced by viscosity and magnetic field (Reynolds *et al.* 2005; Dong & Stone 2009; Ogiya *et al.* 2018). The bubbles are less dense compared to the ambient medium, which gives rise to the buoyancy (Blanton 2004). The gas displaced by the bubble is compressed in X-ray bright rings and remains in pressure equilibrium surrounding the bubbles (Churazov *et al.* 2002). Depending on their radio luminosity, they are classified as radio bright or radio-filled cavities (A2390, Savini *et al.* 2019), radio-dim or ghost cavities (Perseus Cluster, Fabian *et al.* 2002); and intermediate cavities, where the radio emission partly fills the cavity (A4059, Heinz *et al.* 2002). The short radiative lifetime of the cosmic ray electrons (only tens of Myr) makes it challenging to explore these sources in GHz frequency. Low-frequency radio observations with uGMRT, LOFAR can probe the radio emission from the old particle population of the AGN outflows in ghost and intermediate cavities (Russell *et al.* 2019; Bîrzan *et al.* 2020; Biava *et al.* 2021; Brienza *et al.* 2021). Deep radio observations of these sources are needed to establish radio X-ray correlations, which would help in understanding the bubble dynamics, the role of magnetic field and also the feedback mechanism better.

As we are approaching more and more towards lower frequency radio study with telescopes like uGMRT, LOFAR, MWA, SKA-low (in future), many more details about these fossil sources are to be unveiled in coming years, which would improve our understanding of these sources significantly.

3.6 *Magnetic fields in clusters from polarisation studies*

Besides gravity, magnetic fields are also believed to play an important role in the evolution of the ICM. A host of X-ray and radio continuum observations have revealed their physical properties, such as temperature, extent, presence of low Mach number shocks and possible sites of particle acceleration (Enßlin *et al.* 1998; Feretti *et al.* 2012; van Weeren *et al.* 2019).

A clear understanding of the structural nature and the coherence scale of magnetic fields in cluster halos is currently inadequate, and it is thus important to gather knowledge on the factors that drive turbulence in the ICM, and subsequently to understand how they distribute and accelerate relativistic plasma, contribute to pressure balance, and affect the gas content in galaxies (e.g., Donnert *et al.* 2009; Vazza *et al.* 2021a). Much of our knowledge of the cluster magnetic fields comes from the diffuse synchrotron emission from cosmic ray electrons. This emission is expected to be partially linearly polarised (e.g., Govoni *et al.* 2013; Sur *et al.* 2021), and its measurement is capable of providing insights into the properties of the magnetic field structure in ICM.

Magnetic fields in the ICM have been mostly studied via analysis of the Faraday rotation measure (RM) of polarised radio sources lying in the background or embedded within the magnetised ICM (Kronberg 1994; Clarke *et al.* 2001; Murgia *et al.* 2004; Rudnick & Blundell 2004; Bonafede *et al.* 2010; Böhringer *et al.* 2016), the so-called RM-grid. These studies show that the dispersion of RM ($\sigma_{\rm RM}$) decreases substantially as a function of impact distance from the cluster centre, where $\sigma_{\rm RM} \approx 200$ rad m^{-2} towards the centre to $\sigma_{\rm RM} \lesssim 50$ rad m^{-2} at distances $\gtrsim$500 kpc from the centre. By comparing these results with numerical models, which assume Gaussian random distribution of magnetic fields in clusters, evidence for μG-level fields that are ordered on scales of several kpc in the ICM have been found.

RM-grid-type studies are faced with a few challenges. Firstly, it is difficult to disentangle the RM contributed by the ICM from that of the RM intrinsic to the background sources. This might affect the inferred $\sigma_{\rm RM}$, and thereby an accurate understanding of the magnetic field structures in the ICM (Locatelli *et al.* 2018). Secondly, RM-grids are severely limited to only a few, $\mathcal{O}(10)$, background polarised sources per cluster (Bonafede

et al. 2010), which makes constructing a 2-D RM-map arduous. Due to the limited number of Faraday RM measured towards background polarised sources of a cluster halo, the magnetic field along the line of sight in the ICM is discretely sampled and, therefore, background RM data from several clusters are statistically investigated (e.g., Böhringer *et al.* 2016). Thirdly, while the assumption of a Gaussian random magnetic field distribution allows for the power spectrum of the field to be expressed as a simple power-law and subsequently apply to the observed RM data (Clarke *et al.* 2001; Murgia *et al.* 2004; Bonafede *et al.* 2010), this assumption is in complete contrast to the intermittent nature and non-Gaussian distribution exhibited by the field components generated by fluctuation dynamos in the ICM (Seta *et al.* 2020; Sur *et al.* 2021). Thus, a meaningful comparison between numerical predictions and observations of RM is limited by assumptions made about the structure of magnetic fields in the cluster halo. This situation is unlikely to drastically improve, even with the advent of new and sensitive radio telescopes. For a proper quantification of the strength and structure of magnetic fields in the ICM, it is imperative to take into account the other two complementary observables that trace magnetic field structures—synchrotron emission and its polarisation.

Despite years of work, polarised synchrotron emission from the radio halos is yet to be detected convincingly. For a confident detection of polarised emission from the diffuse ICM, the main problems are due to low surface brightness, strong Faraday depolarisation, steep radio continuum spectra of the ICM and confusion from polarised relic emission seen in projection. Based on cosmological magnetohydrodynamic (MHD) simulations, Govoni *et al.* (2013) expect that luminous halos may show a polarised flux density of 0.5–2 μJy at 1.4 GHz when observed with 3 arcsec angular resolution, corresponding to a surface brightness of only 50–200 nJy arcsec^{-2}. Due to the large Faraday dispersion expected in the ICM, Böhringer *et al.* (2016) found that the presence of a cluster medium increases $\sigma_{\rm RM}$ by about 60 rad m^{-2}, and therefore, polarised halo emission is expected to be severely depolarised at 1.4 GHz. Going to higher frequencies ($\gtrsim$2 GHz) to reduce Faraday depolarisation is also challenging, as the surface brightness of the synchrotron emission is further reduced due to the steep radio continuum spectrum ($\alpha \gtrsim 1$) of the ICM emission. Furthermore, since radio relics show substantial polarised emission near 1 GHz (van Weeren *et al.* 2010; Wittor *et al.* 2019; Dominguez-Fernandez *et al.* 2021), even when observations are performed at relatively poor angular resolutions with single-dish telescopes (Kierdorf *et al.* 2017), the tentative polarised emission that have been reported for only three clusters, namely, for Abell 2255 (Govoni *et al.* 2005), MACS 0717.5+3745 (Bonafede *et al.* 2009b) and Abell 523 (Girardi *et al.* 2016) are likely to be related to relics rather than the halo (Pizzo *et al.* 2011; Rajpurohit *et al.* 2021b). Hence, to identify an efficient observing strategy, it is necessary to investigate the properties of the polarised emission using various types of MHD simulations.

3.7 *High frequency radio observations*

The SZ effect produces distortions in the cosmic microwave background (CMB) spectrum through inverse Compton scattering of CMB photons off the energetic electrons present in and around cosmic structures, most notably galaxy clusters (Birkinshaw 1999). The SZ effect is proportional to the pressure (or energy density) of the electron population, and systematically shifts the CMB photons from the Rayleigh–Jeans to the Wien side of the spectrum. The SZ effect due to the thermal population of electrons, such as in the ICM are well characterised through detections in directions of several galaxy clusters (Birkinshaw 1999). It is now well-known that the ICM does not comprise entirely of thermal plasma, but contains relativistic electrons and protons. Thus, the distortions to the CMB spectrum caused by all the populations of electrons (thermal and non-thermal) need to be accounted for. The generalised expression for the SZ effect including combinations of electron populations has been derived by Colafrancesco *et al.* (2003).

The bullet cluster is one of the most spectacular and well-known examples of an energetic cluster merger. It hosts a powerful radio halo in the central region (Malu *et al.* 2016). The 5.5 and 9 GHz detection of diffuse emission from the bullet cluster has been performed with the ATCA. Due to limited short spacing, the images may suffer from missing flux from the diffuse emission. Similar high frequency work has been reported for sausage cluster at 16 GHz (Stroe *et al.* 2014b).

Spectra of radio halos and relics are crucial for constraining models proposed to explain the emission. The spectra are expected to have one or more breaks, where the spectrum is expected to steepen. In addition to these breaks, basic parameters that characterise the energy distribution of the electrons in the atmospheres of the galaxy cluster are the high- and low-energy cut-offs in the spectra of diffuse emission, which consist of non-thermal populations of electrons. For characterising the high-energy cut-offs, high-frequency observations of

diffuse emission in clusters are clearly needed. Only two relics have been imaged in the frequency range of 0.15–30 GHz using a number of radio telescopes (Stroe *et al.* 2016).

The energetics of non-thermal emission depends critically on the minimum energy to which the power-law distribution of relativistic particles is accelerated (Blundell *et al.* 2006). This low-energy/low-frequency cut-off can be found in two ways, through observations of inverse Compton scattering (ICS)—through the ICS emission in X-ray, or through the SZ effect (Basu *et al.* 2016a, b). For non-thermal populations of electrons—as in radio relics, a detection of the SZ effect amounts to the most direct characterisation of this low-energy cut-off. This has been confirmed for relativistic electrons in a radio galaxy jet, for the first time, by Malu *et al.* (2017), through their cm-wave observations. The SZ effect has also been recently used to detect warm-hot intergalactic matter (WHIM, de Graaff *et al.* 2019) through stacking. The characterisation of WHIM and low-energy cut-offs through the SZ effect makes a compelling case for high-frequency (>20 GHz) observations of galaxy clusters—the two physical phenomena are promising techniques for probing the intergalactic/intracluster medium through the SZ effect. These are also relevant for SKA1-mid and -high bands up to 14 GHz. It is critical that SKA1-mid to retain sub-bands up to and above 14 GHz, which will aid to these high-frequency studies of galaxy clusters.

4. Radio emission from poor clusters and groups

Structure formation in the Universe is expected to be self-similar on scales of supercluster filaments down to smaller systems of galaxies (e.g., Kaiser 1986; Morandi & Sun 2016). However, the lower-mass end of these systems (i.e., poor clusters and groups) have not been observed in as much detail as the richer systems, mostly because of the challenges in the observations (e.g., limitations in sensitivity) at various parts of the spectrum necessary for such studies using existing facilities. Earlier studies expressed the expectation that such self-similar properties would be true even for X-ray and non-thermal radio emission (Vikhlinin *et al.* 2006; Cassano *et al.* 2013). The emerging scenario from deeper observations and simulations indicates that such self-similarity might be broken in energy and mass scaling in lower-mass systems (Paul *et al.* 2017; John *et al.* 2019; Lovisari *et al.* 2021 and references therein).

Low-mass clusters and groups are unstable to small mergers, owing to their shallow gravitational potential and are strongly affected by various non-gravitational processes (Lovisari *et al.* 2015). The content of cosmic rays in these systems is high, likely due to the influence of greater AGN feedback activity (Gilmour *et al.* 2009; Li *et al.* 2019). Simulations on the evolution of turbulence and cosmic rays in low-mass objects show that these significantly deviate from the self-similar scaling found in richer clusters, having flatter slopes and higher fluctuations, indicating better visibility of a fraction of them through their non-thermal properties (Paul *et al.* 2017; John *et al.* 2019), such as the radio halo emissions (Paul *et al.* 2018). This may also result in a systematic departure of these sources from the expected scaling relations. Furthermore, the low-mass clusters are usually cooler than the massive ones, the Mach number of a fraction of the merger shocks is expected to be noticeably higher inside the low-mass clusters (Sarazin 2002). This is because, unlike the thermal evolution, merger shock velocity does not directly depend on the mass of the host cluster. However, to examine these observationally, we should have enough data at the lower mass end, currently, which is largely missing in the available literature (see Figure 4 and Section 4.1).

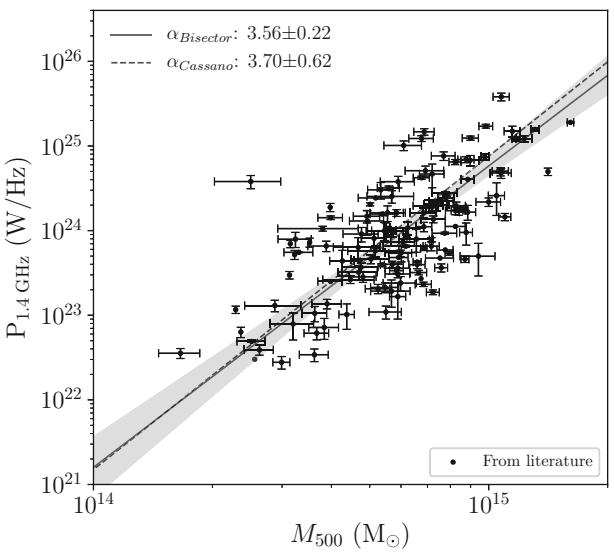

Figure 4. Radio halo power plotted against mass M_{500} of all the radio halos observed so far (van Weeren *et al.* 2019; Cuciti *et al.* 2021b; Paul *et al.* 2021; Botteon *et al.* 2022; Hoang *et al.* 2022). Radio power is scaled to 1.4 GHz, considering the spectral index as available in literature, otherwise the spectral index of −1.3 is assumed.

4.1 *Observations of low-mass clusters and groups*

The environment of poor clusters and groups, dotted on the cosmic web, is the dominant location for the early evolution of galaxies, in contrast to the better-studied rich clusters, which contain only a few percent of galaxies (e.g., Freeland & Wilcots 2011). Galaxy groups are the dominant reservoir of baryons in the Universe, but their shallow gravitational potential is vulnerable to tidal disturbances, galaxy interactions and mergers. Arguably, it is these low-mass systems that hold the key to the understanding of key processes of heating (feedback due to star formation or AGN activity) and cooling, the mechanisms and timescales of energy injection, and the effects of the galaxy and group evolution on the development of the hot intergalactic medium.

For this, the basic observations are a combination of deep X-ray observations of the hot intergalactic medium and radio observations of the synchrotron-emitting plasma associated with AGN activity and star formation. Coupled with these, observations of molecular and atomic gas, and dust yield crucial information.

Deep X-ray observations from Chandra and XMM-Newton are being obtained for a wide range of system masses ($\sim 10^{13}\ M_\odot$ to a few times $10^{15}\ M_\odot$) (Popesso *et al.* 2004; Hofmann *et al.* 2017), of which groups are generally referred to as systems with $\lesssim 10^{14}\ M_\odot$ (Paul *et al.* 2017), and poor clusters ($10^{14}\ M_\odot \lesssim M \lesssim 5 \times 10^{14}\ M_\odot$). For decades, VLA L-band and C-band observations revealed radio sources in central galaxies in low-mass systems (e.g.,Burns *et al.* 1987). The fact that diffuse radio emission was rarely detected in early shallow observations at L-band in such systems led to lack of information about activity of most nuclei in the central galaxies of low-mass systems. As AGN feedback began to emerge as the dominant source of heating in the intracluster gas in rich cluster, there were doubts about the nature of the extra heating in the cores of clusters. However, deeper observations, particularly at lower frequencies, initially with the GMRT, have revealed the presence of these sources in poor clusters, such as AWM4 (O'Sullivan *et al.* 2011b) and groups such as HCG 62 (Gitti *et al.* 2010), NGC 5044 (David *et al.* 2009), NGC 1407 (Giacintucci *et al.* 2012), NGC 741 (Schellenberger *et al.* 2017) and many others (Giacintucci *et al.* 2011; O'Sullivan *et al.* 2011a). In addition, as the relativistic plasma from these AGN becomes older, they lose energy and predominantly radiate at lower frequencies, thus being more prominent in low-frequency observations. Well-defined samples of galaxy groups need to be constructed for multi-wavelength observations to understand the systematics—the optically selected CLoGS study (Kolokythas *et al.* 2022) or the X-ray-selected XXL sample (Šlaus *et al.* 2020) are positive steps in this direction.

The unprecedented sensitivity of LOFAR ($\sim$80 μJy at 144 MHz) and uGMRT ($\sim$20 μJy at band 3) has, however, revolutionised the study of diffuse emission in low-mass systems as observed through individual studies (Botteon *et al.* 2019; Hoang *et al.* 2019; Knowles *et al.* 2019; Paul *et al.* 2020) as well as in a handful of systematic explorations (Paul *et al.* 2021; van Weeren *et al.* 2021; Botteon *et al.* 2022).

Although less numerous, low mass clusters are now detected with almost all types of diffuse radio sources, even the ultra-steep sources (Mandal *et al.* 2020). Particularly, the detection fraction of relics is more in low-mass systems than in high mass systems (e.g., de Gasperin *et al.* 2014, 2017b; Kale *et al.* 2017; Dwarakanath *et al.* 2018). Almost 31% of all diffuse emissions from low-mass systems are cluster-radio shocks (relics) compared to only 21% in high mass systems, as observed by Botteon *et al.* (2022) in their large sample of 146 clusters with mass $M < 5 \times 10^{14}\ M_\odot$ and 135 high mass systems from the Planck cluster list. So far, the lowest mass galaxy cluster known to host radio relics is Abell 168 (Dwarakanath *et al.* 2018) with a mass $M \sim 1.24 \times 10^{14}\ M_\odot$. From the correlations of radio halo power vs halo size and radio halo power vs mass (Cassano *et al.* 2007, 2013; Feretti *et al.* 2012; Cuciti *et al.* 2021b), it can be inferred that radio halos detected in poor clusters are usually smaller in extent. However, a rare giant halo of size $\sim$750 kpc has been detected by Botteon *et al.* (2021) in one of the lowest mass ($\sim 1.9 \times 10^{14}\ M_\odot$) clusters PSZ2G145.92−12.53 using the LoFAR. It is also known to be the lowest power radio halo detected so far. Since low-mass galaxy clusters are mostly dominated by the AGN activities, the dying component, such as AGN relics with ultra-steep spectrum nature have been detected in some of them (e.g., Brüggen *et al.* 2018; Mandal *et al.* 2020). Nikiel-Wroczyński *et al.* (2019) even reported the detection of diffuse emission from the intergalactic medium in compact galaxy groups. With these discoveries, researchers have demonstrated that low-frequency telescopes like uGMRT and LoFAR have huge potential to detect diffuse cluster radio sources, even in low-mass to group scales.

The existing radio halo power mass correlation ($P_{1.4\ \mathrm{GHz}}$–M_{500}) shows a steep spectrum (slope $\sim$4) and bi-modal distribution in radio power–X-ray ($P_{1.4\ \mathrm{GHz}}$–L_X) plane (Cassano *et al.* 2013), predominantly with the massive objects. With the previous (for a review,

van Weeren *et al.* 2019 and references therein) and more recent observations (Cuciti *et al.* 2021b; Paul *et al.* 2021; Botteon *et al.* 2022; Hoang *et al.* 2022) available in literature that revealed a sizable number of new radio halos and relics, some even in low-mass clusters (Paul *et al.* 2021; Botteon *et al.* 2022; Hoang *et al.* 2022), we re-plot and estimate the correlation for $P_{1.4\ \mathrm{GHz}}$–M_{500}. Since, the diffuse emission from many of the galaxy clusters have been observed in different radio frequency bands, to be consistent with the estimates reported in literature, the halo radio power is scaled to 1.4 GHz, assuming the spectral index of −1.3 (unless the spectral index is available in literature). The updated correlation plot is shown in Figure 4. The BCES bisector slope for $P_{1.4\ \mathrm{GHz}}$–M_{500} ($\alpha_{\mathrm{new}} = 3.56 \pm 0.22$) by and large follow the Cassano *et al.* (2013) correlation ($\alpha = 3.70 \pm 0.56$). However, the slight flattening of the slope, and lack of data points below the mass $M < 4 \times 10^{14}\ M_{\odot}$, motivate for more systematic and dedicated studies at the lower mass end.

5. Superclusters and filamentary cosmic web

Superclusters of galaxies consist of galaxy clusters with linear or sheet-like inter-cluster filaments, corresponding to the denser crossroads of the cosmic web (e.g., Cautun *et al.* 2014) with groups of galaxies embedded in them. These are the most extensive and massive systems ($\geq 10^{16}\ M_{\odot}$) in the Universe that have decoupled from Universal expansion and are collapsing, significant parts of them are being gravitationally bound. Cosmological *n*-body simulations and observations, both support that strong concentrations of matter appear to be interconnected by vast, low-density filaments surrounded by volumes that are devoid of galaxies, which are identified as voids.

5.1 *Superclusters of galaxies*

In redshift surveys of galaxies and clusters, several well-known large-scale structures that can be called superclusters according to the description above, have been identified. These include the Corona Borealis supercluster (Postman *et al.* 1988), the Coma supercluster (de Lapparent *et al.* 1988; Mahajan *et al.* 2011), Hydra-Centaurus supercluster (da Costa *et al.* 1986), Pisces-Cetus supercluster (Porter & Raychaudhury 2005), Hercules supercluster (Tarenghi *et al.* 1979), Shapley supercluster (Raychaudhury 1989; Day *et al.* 1991; Raychaudhury *et al.* 1991) Saraswati supercluster (Bagchi *et al.* 2017) and our very own Laniakea supercluster (Tully *et al.* 2014), of which the local group is a part, and many others that have been catalogued (e.g., Bahcall & Soneira 1984; Liivamägi *et al.* 2012; Tempel *et al.* 2014). Observations of superclusters are very important as they provide crucial information about the early evolution of structures in the Universe, and formation and early evolution of galaxies, which spend most of their lives in this environment.

One of the important aspects of studying such filamentary superclusters is to trace the large scale shocks that pass through the ICM (or intergalactic medium, IGM), and their effect on the formation of the complex cosmic web (Miniati *et al.* 2000; Ryu *et al.* 2003; Pfrommer *et al.* 2006). Numerical simulations reveal different kinds of shocks, which control the overall evolution of large scale structure. These mainly belong to two categories: 'internal' and 'external' shocks. The former (internal or merger shocks) affect the material that is already heated to approximately the cluster temperature ($\sim 10^7$ K) and may be responsible for generating cluster scale ($\sim$1 Mpc) diffuse radio sources in the form of halos and relics (mostly in massive clusters). The latter kind (external or accretion shocks) is responsible for heating the cold gas surrounding the cluster out to the virial radius, and may be associated with infall of matter along the filamentary web surrounding the cluster (Hoeft & Brüggen 2007; Paul *et al.* 2011).

The merger shocks have a low Mach number ($\mathcal{M} \sim 2$–3), while accretion shocks have a high Mach number ($\mathcal{M} \sim 10$–10^2). Such infall velocities are high enough that the infalling material can be accelerated to total energies of 10^{18}–10^{19} eV, while accreting onto collapsing structures. In the presence of even a weak magnetic field (10–100 nG), where the energy density of the magnetic field accounts for only 1% of the total post-shock energy density, it is possible to detect the radio synchrotron emission that couples with accretion shock (Wilcots 2004). Thus, sensitive and high-resolution radio observations of superclusters can be useful to probe the underlying distribution of cosmic rays and magnetic fields (Miniati *et al.* 2000; Vernstrom *et al.* 2017).

Simulations (Araya-Melo *et al.* 2012; Vazza *et al.* 2012b) predict that it is possible to detect extended diffuse radio sources associated with filaments if the shocks accelerate the electrons sufficiently (Keshet *et al.* 2004). Vacca *et al.* (2018) have already detected, using the Sardinia Radio Telescope at L-band, a new population of faint and diffuse 28 candidate radio sources associated with a large scale filament. They have identified nine massive clusters ($z \sim 0.1$) surrounding filaments in their survey area, which covers $8^\circ \times 8^\circ$. The sizes of these radio sources vary from 0.3 to 8.6 Mpc.

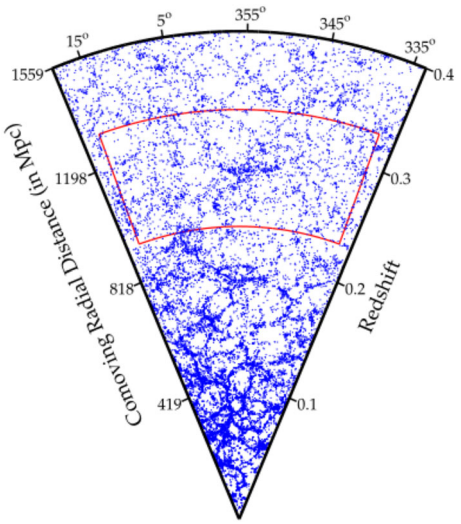

Figure 5. Redshift cone plot for the Saraswati supercluster contains SDSS galaxies from $z = 0$–0.4. The red box shows the concentration of galaxies of the Saraswati supercluster of width in RA 45° and Dec 2.5° (which is not shown for clarity). This figure is taken from Bagchi *et al.* (2017).

The mean radio power and mean X-ray luminosity of these new radio sources are 10–100 times lower than those of diffuse radio emissions normally associated with clusters. Moreover, superclusters are promising targets to attempt the detection of the very challenging warm–hot intergalactic medium (WHIM) in radio bands, which shed light on shock-heated collapsing diffuse intergalactic medium (IGM) in filaments (Cen & Ostriker 1999; Tripp *et al.* 2000). To accurately map the 'Cosmic web' after subtracting the confused foreground or background compact radio sources, we need high surface brightness sensitivity ($<\mu$Jy arcsec^{-2}) and sub-arcsec resolution of the SKA.

As a part of the radio observations of a supercluster with future generation radio telescopes, we are studying one of the extensive superclusters Saraswati with MeerKAT and uGMRT. The Saraswati supercluster was identified in the stripe 82 SDSS region, at redshift $z \sim 0.3$ (Bagchi *et al.* 2017). The total mass and size of this supercluster are $\sim 2 \times 10^{16}\ M_{\odot}$ and ~200 Mpc, respectively, making it one of the largest observed structures in the Universe. Figure 5 shows how SDSS galaxies are distributed in the Saraswati supercluster in a redshift cone plot (taken from Bagchi *et al.* 2017). As seen in this plot, the Saraswati supercluster is situated (red box) within $336° < \text{Ra} < 16°$, $-1.25° < \text{Dec} < 1.25°$ in the 270 degree^2 equatorial Stripe 82 region. In sensitive MeerKAT L-band pilot radio observations of the Saraswati supercluster (Parekh *et al.* 2022), our primary aim is to detect faint and diffuse radio sources associated with filaments and study their properties.

5.2 *Radio ridges in interacting clusters*

Apart from radio halos and relics as described above, due to the filamentary nature of the cosmic web, large-scale diffuse radio sources are also detected beyond the main extent of galaxy clusters at the outskirts, where the electron density is very low as compared to the cluster core. These rare, steep spectra and low-surface brightness radio sources could be well detected with low-frequency radio observations. Such 'radio ridges' have now been detected in only a few systems, as filaments between pairs of merging clusters (Botteon *et al.* 2018, 2020b; Govoni *et al.* 2019; Venturi *et al.* 2022).

The first low surface brightness radio ridge of this kind was found in the Coma supercluster, connecting the central halo and the outer relic (Kim *et al.* 1989). The corresponding X-ray observation (of the Coma cluster) suggests the moderate correlation between X-ray and radio brightness of the Coma bridge. Also, the effect of the flow of the cold diffuse gas, down the filaments connecting the clusters in the supercluster can be seen in the star formation properties of galaxies in the Coma and A1367 clusters (e.g., Seth & Raychaudhury 2020). This further indicates that the X-ray and radio emission are generated from the same volume and there is no projection effect.

Among the most notable discoveries in this genre is the spectacular ~5 Mpc size radio ridge connecting the two massive clusters A399 and A401 (Govoni *et al.* 2019), discovered with the Low-Frequency Array (LOFAR) (van Haarlem *et al.* 2013) at 144 MHz frequency. Previously, X-ray observations of the A399–A401 galaxy cluster have revealed a hot (6–7 keV) X-ray filament between the pair (Fujita *et al.* 2008). Moreover, (Murgia *et al.* 2010) detected radio halos with each of the clusters at their centre.

The detailed morphology of the cosmic web shows rich large-scale structures of interconnecting filaments with clusters and groups embedded in them, and the interaction of warm and cold gas on these filaments is likely to have a profound influence on the regulation of star formation in the early life of galaxies (e.g., Pimbblet *et al.* 2004; Mahajan *et al.* 2012). In the core of the Shapley supercluster, Breen *et al.* (1994) had pointed out a chain of four merging clusters (the central cluster A3558, group SC1327-312, group SC1329-313 and A3562, from Einstein and ROSAT observations.

Recently, Venturi *et al.* (2022), using high sensitive MeerKAT L-band data, reported the first GHz detection of inter-cluster diffuse emission (∼1 Mpc scale) joining A3562 cluster and group SC1329-313 along this filament. This bridge has not been detected in previous radio observations, only being detected in the deep MeerKAT data. This certainly points to further possibilities of direct discovery in supercluster filaments along the cosmic web filaments. Another spectacular example is that of ZwCl 2341.1+0000, a complex merging structure of galaxies located at $z = 0.27$, where a system of three merging clusters along with radio and X-ray emitting ridges are found, along with post-merger relics, as the heart of the Saraswati supercluster (Bagchi *et al.* 2002; van Weeren *et al.* 2009).

The origin of radio synchrotron emission from these radio ridges is not well understood. The radiating timescale of electrons at 140 MHz is short, and they can travel only a distance of <0.1 Mpc in their lifetime. On the other hand, the sizes of radio ridges are $\gtrapprox$ Mpc, which suggests *in situ* particle re-acceleration mechanism required for the radio ridge emission. Simulations have revealed a dynamically complex structure of radio ridge in which a shock acceleration mechanism, due to a cluster merger, is not the main source of the observed radio emission (Govoni *et al.* 2019), as is the case with radio relics. It is rather a turbulence in the inter-cluster bridge, caused by complex substructures embedded between galaxy clusters. This turbulence produces weak shocks ($\mathcal{M} \leq$ 2–3) that cause re-acceleration of the pre-existing fossil electrons of energies (∼ GeV), which interact with the (∼ nG) magnetic fields and generate radio emission. Brunetti & Vazza (2020) have predicted that the Fermi(II) re-acceleration mechanism is most favoured under these physical conditions and gives rise to long dynamical time scales of radiating electrons in the bridges connecting clusters. Observing this type of radio object is a major challenge due to its truly diffuse nature on such large spatial scales. We are interested to observe X-ray selected binary merging clusters (which also have hot X-ray filaments) with new radio telescopes, such as MeerKAT and uGMRT to detect the radio ridges and probe their properties (Parekh *et al.* 2017a, 2019, 2020).

6. Theoretical models and efforts on simulating cluster radio emissions and magnetic fields

The diffuse radio emissions found in the cluster medium are theoretically understood to be generated due to synchrotron radiation from GeV electrons in a magnetised medium (Giovannini & Feretti (2000) and for review, Ferrari *et al.* (2008); Brunetti & Jones (2014) and references therein). Therefore, the detection of these diffuse radio structures in clusters provides indirect evidence for the non-thermal component of cosmic rays as well as the magnetic field in the ICM (e.g., Large *et al.* 1959; Willson 1970). Cosmic rays are usually the charged particles re/accelerated due to the merger driven shocks and the turbulent flows in the ICM. The particle (re-acceleration supposedly happens either from the ICM thermal pool, pre-existing electrons or the radio quite AGN lobes through two well-known processes, namely Fermi acceleration of orders one and two. Although the entire processes are difficult to unfold directly from observations, in recent decades, the cosmological simulations of clusters of galaxy formation are a leap forward in understanding the processes quantitatively.

6.1 *Diffusive shock acceleration (Fermi-I)*

The diffuse radio emission at the periphery of the galaxy cluster has a morphology similar to the shock fronts in cluster simulations (Ryu *et al.* 2003; Skillman *et al.* 2008, 2011; Vazza *et al.* 2011; Paul *et al.* 2011), which closely correlate the radio relics to the merger shocks. At the shock fronts, a small fraction of thermal electrons gets accelerated to relativistic energies, known as the diffusive shock acceleration (DSA) mechanism, which in turn emits synchrotron radiation. In the DSA process, the charged particles temporarily get trapped inside the shock region and gain energy each time they reflect back to the upstream (pre-shocked) region across the shock (Drury 1983; Blandford & Eichler 1987; Jones & Ellison 1991; Malkov & Drury 2001). The magnetic field perturbations induced by plasma effects in shock-medium, accelerate the electrons by reflecting back to the upstream, this process is also known as the first-order Fermi mechanism. These accelerated electrons in the presence of compressed magnetic fields emit synchrotron radio emissions along the shock surface and its downstream, which can successfully explain the elongated diffuse radio structures at clusters scales, known as the radio relics (as discussed above). According to Drury (1983) and Blandford & Eichler (1987), for a planar steady shock, the electrons that are accelerated (via Fermi first-order process) by the shock of Mach number $\mathcal{M}$ form a power-law distribution in momentum space:

$$f(p) \propto p^{-q}; \quad q = \frac{4\mathcal{M}^2}{\mathcal{M}^2 - 1}. \tag{1}$$

With this, the radio synchrotron spectrum due to these accelerated electrons follow the power-law $S_\nu \propto$

$\nu^{-\alpha_{inj}}$, with spectral index:

$$\alpha_{inj} = \frac{\mathcal{M}^2 + 3}{2(\mathcal{M}^2 - 1)}, \quad (2)$$

while the volume integrated radio spectrum becomes $S_\nu \propto \nu^{-\alpha_{\rm int}}$, where $\alpha_{\rm int} = \alpha_{inj} + 0.5$ (Enßlin *et al.* 1998; Kang 2011). The observed radio spectral index at the shock surface is often compared with the theoretical spectral index to infer the Mach number of the shocks.

The particle acceleration efficiency is constrained to the particle acceleration from the thermal pool. Recent studies by Botteon *et al.* (2016); Eckert *et al.* (2016) and Hoang *et al.* (2017) indicate that the particle acceleration from the thermal pool requires large acceleration efficiencies to produce total radio luminosity of the radio relic. Again, Botteon *et al.* (2020a) in his study, tested the scenario with 10 well-studied radio relics, where shocks were observed in X-rays as well. They calculate the electron acceleration efficiency of these shocks if injected from the thermal pool, to reproduce their observed radio luminosity. And report that the standard DSA model cannot explain the origin of the relics if efficiency is $<10\%$, as constrained by the studies of SN-driven shocks in galaxies. Whereas, SN-driven shocks are very strong with a high Mach number ($>10^2$) and are also found in a low beta-plasma ($\beta =$ gas pressure/magnetic pressure). In contrast, the shocks in ICM are much weaker, where ICM plasma has high beta $\sim$100 (Kang *et al.* 2014).

6.2 *Shock detection in cosmological simulations*

Cosmological simulations are essential to closely study shocks resulting from cluster mergers. Identifying shock structures in simulations is crucial, but significant to understand the kinetic energy flux mediation through shocks in the ICM. A fraction of the shock kinetic energy thermalizes the ICM, and helps in achieving the virialisation state. The remaining energy results in the production of cosmic-ray particles (protons or electrons) through the first-order Fermi mechanism.

In the literature, there are a few grid-based methods (Miniati *et al.* 2000; Ryu *et al.* 2003; Skillman *et al.* 2008; Vazza *et al.* 2011, 2018) and in SPH code (Pfrommer *et al.* 2006; Hoeft *et al.* 2008) that identify the shocks and its magnitude, i.e., the associated Mach number, using the Rankine–Hugoniot jumps conditions across the shocks. Miniati *et al.* (2000) and Ryu *et al.* (2003) attempt to identify the shock in the 'single-grid' codes and estimate the shock Mach number using temperature jump condition. They marked the shocks as 'accretion shocks', where for the first time the photo-ionised gas is shock-heated and 'merger shocks', where the pre-shock gas has previous shock encounter(s). In addition, Ryu *et al.* (2003) accounts for the floor temperature of intra-galactic medium (IGM), i.e., the minimum gas temperature, $T_{\rm min} \approx 10^4$ K, created by the re-ionisation of stars. This prevents us from over-estimation of the accretion shock strength in adiabatic simulations. The obliquity of the shock, multiple shock cells and directional dependence in the shock cells are the significant issues to address. Ryu *et al.* (2003) adopts the co-ordinate split approach to estimate the shock Mach number, whereas Skillman *et al.* (2008) determine the shock strength in the direction of shock propagation. Skillman *et al.* (2008) made the first attempt to study the shock in adaptive mesh refinement grid-based code, where the former attempts are on uni-grid-simulations, and report that the previous methods (Ryu *et al.* 2003) overestimate the number of low Mach number shocks by a factor of $\sim$3 due to the misconception about the direction of shock propagation. Later, Vazza *et al.* (2011) compute the shock strength using the velocity jump criterion, which is very well consistent with the temperature jump criterion, except, the velocity jump method is more reliable at the outskirts of galaxy clusters or low-density environment in estimating the Mach number. All above-discussed shock detection schemes identify the shock and its strength as a post-process, which may cause uncertainties in the characterisation of shocks since they consider the ideal conditions across the non-shocked-cells, i.e., no velocity and no temperature gradients, which already exist in a complex cosmological flow (in velocity and temperature fields) wherein the thermodynamic gradients due to shock are superimposed (Vazza *et al.* 2011). It demands the run-time shock detection to overcome the uncertainties, Vazza *et al.* (2018) attempt to hastily identify the shock, in a grid-based adaptive-mesh refinement (AMR) simulation code (ENZO), moreover, introduce a method to increase the level of refinement at the locations of shock fronts. Where, the AMR criterion based on one-dimensional velocity jump is added to the usual AMR criteria as adopted for gas and dark matter over-density in O'Shea *et al.* (2004). Additionally, in Vazza *et al.* (2018), the total shock strength is estimated by the pressure jump conditions, which account for the feedback from cosmic-ray flux at the shock fronts. Even hydrodynamical cosmological simulation basically describe the merger shocks, achieving sufficient numerical resolution, and locating the shock fronts and their strength is still a challenge.

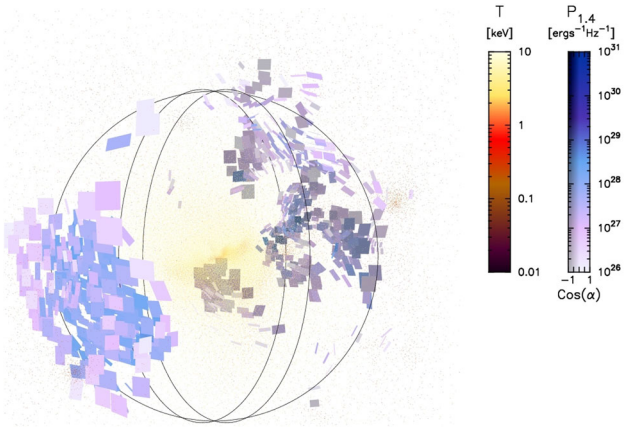

Figure 6. This is an example of double relic (figure taken from Hoeft *et al.* (2008)), representing two large shock fronts on the cluster periphery, from the SPH-MareNostrum Universe simulation. This shows the spherical nature of shocks, very similar to the radio relics found in Abell 3667 and Abell 3376.

6.3 *DSA in cosmological simulations*

In the last decade, many attempts were made to estimate the synchrotron radio emission from the shock waves (Hoeft & Brüggen 2007; Hoeft *et al.* 2011; Skillman *et al.* 2011; Nuza *et al.* 2012, 2017; Paul *et al.* 2018, 2020; Wittor *et al.* 2019, 2021a, b; Brüggen & Vazza 2020). The widely used semi-analytical solution to compute the total monochromatic radio power at frequency ν from a shock wave of area A, having electron efficiency ξ_e, with the downstream temperature T_d, the downstream electron density n_d and magnetic field strength B, have been derived by Hoeft & Brüggen (2007) as:

$$P(\nu) \propto A n_d \xi_e \nu^{-\alpha_{\rm int}} T_d^{\frac{3}{2}} \frac{B^{1+\alpha_{\rm int}}}{B_{\rm CMB}^2 + B^2}, \qquad (3)$$

where $B_{\rm CMB}$ is the magnetic field corresponding to the energy density of CMB. Equation (3) enables one to implement it as a post-process to estimate the radio power in any cosmological/galaxy cluster simulation (e.g., Figure 6). The underlying assumptions to derive this relation is that the electrons (i.e., with minimum momentum, say $p_{\rm min}$) from the thermal pool, having Maxwellian distribution, get accelerated by the shock to a power-law distribution, which is closely related to the Mach number of the shock (DSA theory). These accelerated electrons emit in radio through synchrotron process in a magnetised medium.

If one performs MHD simulations, the magnetic field strength as direction, is the associative property of the cell in grid simulations (e.g., ENZO), else the approach will be to govern the magnetic field strength using semi-analytical methods (e.g., Roettiger *et al.* 1999). The magnetic field strength is related to the baryonic matter density, i.e., modelling magnetic field strength with density (Bonafede *et al.* 2009a; Skillman *et al.* 2011) and modelling the magnetic field density with turbulence energy density of the medium (e.g., Subramanian *et al.* 2006; Beresnyak & Miniati 2016; Paul *et al.* 2018). Paul *et al.* (2018) demonstrated that the magnetic field in the ICM using magnetic energy density's sub-equipartition with turbulence energy density successfully explains the cluster scale magnetic field. They compare the magnetic field radial profile of the simulated coma-cluster like environment, which is in good agreement with the radial profile studied using the Faraday rotation measure (RM) (Bonafede *et al.* 2009a).

Still, the DSA mechanism is poorly understood. The bottleneck is the minimum momentum required for the thermal electron to accelerate it to relativistic, non-thermal distribution and the efficiency of the shock to accelerate the sufficient charge particles for radio emission.

There are some more puzzles yet to address in DSA. If every shock can produce relativistic electrons from the thermal pool, then correspond to the shocks for every merging cluster, there should be the associated radio relics. However, only a few per cent of merging clusters host the radio relics (Feretti *et al.* 2012). Furthermore, not all X-ray detected shocks show the signature of diffuse radio relics. Moreover, in some relic structures, the strength of the X-ray Mach number computed from the density/temperature jump does not agree with the radio-Mach number estimated from the radio spectral index. To address these puzzles, several authors (Kang & Ryu 2011; Kang 2012; Pinzke *et al.* 2013; Kang & Ryu 2016) proposed the re-acceleration model in which the seed electrons are not from the thermal pool, instead they are considered to be pre-existed in the ICM as fossil electrons as the leftover of radio jets or lobes of the radio-quiet AGN. These radio-quiet electrons may be reborn as radio phoenix if re-accelerated by the merger shocks (also known as the adiabatic compression process) (Enßlin & Gopal-Krishna 2001). The re-acceleration model is quite consistent with the observed radio relics, where the X-ray Mach number shows a discrepancy with radio spectra-derived Mach number (e.g., toothbrush radio relic, Kang & Ryu 2016). This confirms the strong connection between the fossil electrons from AGN and shock acceleration in ICM, provided the cluster must host an AGN (radio-quiet?) like in the case of toothbrush radio relic (van Weeren *et al.* 2016).

6.4 *Turbulence re-acceleration mechanism*

Mergers of two or more galaxy clusters and motion of sub-halo(s) in cluster/halo deeply stir the ICM, i.e., from core sloshing and shear instabilities. The signatures of the ICM turbulence are largely observed in many numerical simulations (Maier *et al.* 2009; Schmidt *et al.* 2009; Iapichino *et al.* 2010; Ryu *et al.* 2010; Iapichino 2011; Paul *et al.* 2011; Vazza *et al.* 2011, 2012, 2017; Federrath *et al.* 2021) of galaxy clusters. Although there are a few attempts of quantifying the turbulence in merging clusters using X-ray observations (e.g., Roncarelli *et al.* 2018). The turbulence motion in clusters of galaxies is defined by its scale, which is almost comparable to the size of cluster cores. Although turbulence in the ICM is majorly subsonic, but is sufficient to translate to MHD turbulences well below the scale at which the Alfvén-velocity equals the turbulent velocity. Studies indicate that these turbulent motions are super-Alfvénic, with Alfvénic Mach number, $M_A \gtrsim 5$ (Brunetti & Lazarian 2007). For the assumed ICM conditions, i.e., $B = 1\,\mu$G, $n = 10^{-3}$ cm, $T = 10^8$ K and $\beta_{\rm plasma} \approx 250$, in the schematic diagram of turbulence energy over wavenumber (Figure 7) the transition region (dark grey) from hydro to magneto-hydro turbulence has been shown (Donnert & Brunetti 2014).

In addition, the plasma instabilities in the ICM results in various kinds of waves, i.e., slow-mode, fast-mode, Alfvén-mode and a few self-excited modes—slab and whistler. These modes are widely explored for the particle (re)-acceleration mechanisms to explain the radio halo-like emission. The term (re)-acceleration by the plasma driven turbulence is coined here because, the acceleration of charged particles to relativistic energies, directly from the ICM thermal pool, is quite inefficient, rather re-acceleration of pre-existing high energy particles is more efficient. In these stochastic re-acceleration processes, the particles drain energy from plasma turbulence due to resonant interaction with the MHD waves (excited due to plasma instabilities).

In the last few decades, the Alfvén-mode and fast-mode are widely explored to understand particle acceleration. In incompressible turbulence, below the Alfvén scale, the acceleration is driven by the Alfvén-mode via gyro-resonance (Yan & Lazarian 2002; Fujita *et al.* 2003; Brunetti *et al.* 2004). It efficiently re-accelerated the relativistic protons and the relativistic electrons, but the acceleration of charged particles, directly from the thermal pool, is possible only for the thermal protons. The duration of the non-thermal process in clusters of galaxies is largely limited by the back-reaction

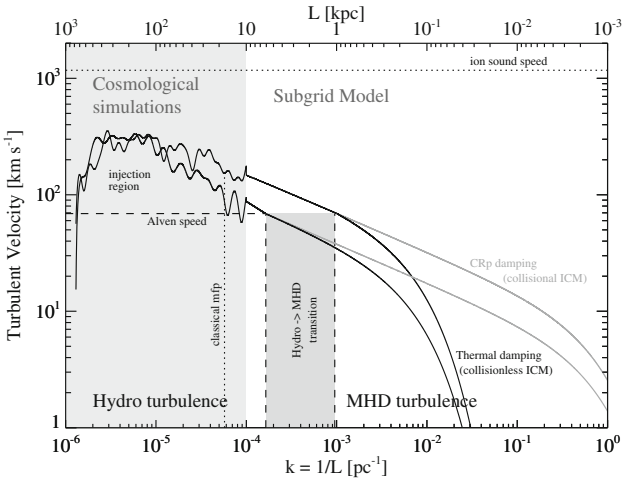

Figure 7. Schematic of the simple turbulence model with standard cluster parameters: $B = 1\,\mu$G, $n = 10^{-3}$ cm, $T = 10^8$ K and $\beta_{\rm plasma} \approx 250$. The classical mean free path $\approx$ 200 kpc, sound speed $c_s = 1200$ km s^{-1} and Alfvén speed ≈ 100 km s^{-1} are shown. The Kraichnan turbulence scaling below the simulation scale $\approx$100–10 kpc is assumed here. In the case of collisional damping, the turbulence cascade damped later, hence, the spectrum extends towards smaller scale (grey line) and CR-electrons re-acceleration becomes more efficient. The figure is taken from Donnert & Brunetti (2014).

of protons on the MHD wave, which suppresses the efficient acceleration of relativistic electrons. Alfvén acceleration indicates a temporal correlation between the dynamical timescale of merger events and the acceleration timescale of electrons, which is estimated to be one order of magnitude shorter than the former one (Brunetti *et al.* 2004). In another scenario, the fast-mode induced in the compressible turbulence driven at large scales in the ICM can re-accelerate the cosmic-ray (CR)-electrons to very high energies ($\approx$a few GeV) via transit-time-damping (TTD) resonance (Yan & Lazarian 2004; Brunetti & Lazarian 2007, 2011a, b; Yan *et al.* 2008). It assumes quasi-isotropic turbulence cascade and high beta plasma ($\beta_{\rm plasma}$, ratio between plasma pressure to magnetic pressure). The coupling between the magnetic moment of charged particles and the parallel magnetic field gradients essentially causes the acceleration of charged particles. The damping of the compressible turbulence can be with thermal particles and relativistic particles. Figure 7 (Donnert & Brunetti 2014) illustrates that the damping rate with thermal particles (dark full line) is higher than the relativistic particles (light grey line), hence at small scales, the cosmic ray re-acceleration becomes more efficient. In all these cases, the acceleration efficiency is constrained by the damping of the turbulence by CR

particles themselves. This modifies the spectrum of the turbulence, and hence, the acceleration efficiency (as back-reaction). However, it is still unclear whether such small-scale waves can efficiently be generated in the ICM or not.

One can understand these mechanisms by studying them in controlled large scale cosmological simulations. In one case, this can be achieved by adopting an analytical or a semi-analytical approach, where the power-law for the particle spectra is estimated to be $n_e(E_e = p_e c) \propto E_e^{-\delta}$, with the assumed turbulence spectra and the fixed turbulence energy injection, and subsequently compute the radio synchrotron emission using Equation (4) as post-processing on each grid-cell in the cosmological simulation to extract the synthetic synchrotron brightness map (Fang & Linden 2016; Paul *et al.* 2018). The synchrotron emission at frequency, ν, is given as (Rybicki & Lightman 1986; Longair 2011):

$$I_\nu = \frac{\sqrt{3} e^3 B}{m_e c^2} \int_{E_{\min}}^{E_{\max}} \int_0^{\frac{\pi}{2}} dE_e d\theta \sin^2\theta F\left(\frac{\nu}{\nu_c}\right) n_e(E_e), \tag{4}$$

where θ is the pitch angle, $F(x)$ is the synchrotron kernel and ν_c is the critical frequency:

$$\nu_c = \frac{3}{2}\gamma^2 \frac{eB}{m_e c} \sin\theta \tag{5}$$

and B is a tangled magnetic field. Here, time-evolution of the spectra is not assumed/studied and estimations are drawn at the frozen epoch of large scale structures in cosmological simulations. On the other hand, significant deviations from the power law for the particle spectra are expected during the time evolution. Hence, numerically solving the Fokker–Planck equation to account for the re-acceleration of every particle in the dense gas in the computational domain is essential for more accurate insight. In this direction, Donnert *et al.* (2013), for the first time, attempted to include the complex CR electron re-acceleration physics into the Smooth Particle Hydrodynamical (SPH) Simulations. They simulate the cosmological flow with high Reynolds numbers to follow the rise and decay of turbulence in the cluster. The evolution of CR electrons is computed in post-processing with all relevant losses and stochastic re-acceleration processes (TTD damping of compressive turbulence in the ICM) by solving the Fokker–Planck equation for every SPH particle. In key observable of their work, in the different states of the merger evolution, they get the variety of observed radio spectra, i.e., flatter, curved and ultra-steep spectrum halos. Interested readers can also refer Donnert & Brunetti (2014) for more insight in numerical solution to the Fokker–Planck equation (Equation (1) of Donnert & Brunetti 2014) and a sub-grid model for compressible MHD turbulence in the ICM (Figure 7).

In the turbulent re-acceleration mechanism, to estimate well-motivated particle-acceleration coefficients and subsequent turbulence scale in different cosmological simulations, one needs to estimate the local turbulence velocity. One simplistic and physically motivated estimate can be the root-mean-square of the velocity dispersion inside the kernel, i.e., subtracting the bulk flow (the weighed or non-weighed average of velocity components) inside the kernel and the root-mean-square of this quantity signifies the turbulent velocity (see in SPH simulations: Vazza *et al.* (2017); Donnert & Brunetti (2014), Grid-based simulations: Vazza *et al.* (2009b, 2015); Paul *et al.* (2018)). The power spectrum of the velocity field of the simulated ICM can be estimated by applying the standard FFT algorithm to the data at the highest available resolution (Federrath *et al.* 2008; Vazza *et al.* 2009b; Vazza 2010; Valdarnini 2011), which describes the type of turbulence-induced in the ICM. Vazza *et al.* (2012) adopted the multiscale filtering algorithms to identify the turbulent motions in hydrodynamical grid simulations (ENZO and FLASH). Most recently, Federrath *et al.* (2021) performed the world's largest, highest-resolution simulations of turbulence in interstellar gas and molecular clouds. It allows to determine the position and width of the sonic scale, which was found to be very close to the theoretical predictions. For the first time, it enables researchers to draw a strong conclusion on the important transition of turbulence from supersonic to subsonic region. Although the initial aim of the simulation is to understand the impact of the turbulence on star formation in molecular clouds, it is the biggest forward leap in understanding the turbulence at sonic scales (3D animation available online).

6.5 *Secondary electrons as source of synchrotron emission*

As an alternative to the turbulent re-acceleration as the source of high energy (GeV) electrons, the hadronic or secondary model has been proposed to account for the production of diffuse radio emission in clusters of galaxies (see e.g., Pfrommer & Enßlin 2004a; Keshet & Loeb 2010). This was conceptualised mainly to explain the Mpc scale size of the radio halos that spans almost the entire cluster volume. Similar to volume filling turbulence, cosmic-ray protons are believed to fill the entire cluster volume (Enßlin *et al.* 2011;

John *et al.* 2019) and can act as the constant injection source for long sustaining emission. The relativistic protons can be produced by the acceleration of thermal proton population by the shocks associated with cosmological structure formation (such as Fermi first-order acceleration mechanism at shock fronts), galactic wind, injection by supernovae and the AGN (Enßlin *et al.* 1998; Völk & Atoyan 1999; Ryu *et al.* 2003, for a review, see Brunetti & Jones 2014). High energy electrons (or cosmic-ray electrons) responsible for synchrotron radio emission are the decay products (or the secondary particles), produced during the inelastic collision between these relativistic protons and the thermal ions in the ICM (Dennison 1980; Schlickeiser *et al.* 1987; Blasi & Colafrancesco 1999; Dolag & Enßlin 2000).

The hadronic model somewhat resolves the difficulty in explaining the size of radio halos (∼1 Mpc); i.e., the required diffusion time for the relativistic electrons to reach such large distances, which is much larger than their radiative lifetime. Since the radiative losses for protons are very low in comparison with electrons, and therefore, the lifetime of CR protons is much longer than that of CR electrons. It makes these relativistic protons to diffuse to very large scales and hence, can accumulate in the cluster environment for a long time. The basic idea of the hadronic model is the continuous injection of CR electrons in the ICM, happening through secondary processes that can successfully explain the sizes of radio halos.

To numerically simulate the radio synchrotron emission implementing the hadronic model, first, the power-law spectrum of the CR protons has been considered. The spectrum of the secondary electrons was then estimated from the proton–proton collisions (Pfrommer & Enßlin 2004b; Brunetti & Blasi 2005; Donnert *et al.* 2010a, b). Donnert *et al.* (2010a) simulated a scenario similar to that of Coma cluster, and numerically predict the radio synchrotron emission from that model cluster, assuming the hadronic scenario. They report that the purely hadronic model disfavours the current radio-halo observations of the Coma cluster. It failed to explain the observed high-frequency spectral steepening of the detected radio halo. Moreover, the model was found incapable of explaining the observed general properties of giant radio halos, such as the observed radio bi-modality in the radio-X-ray correlation plot (Cassano *et al.* 2013), as well as, the overall spectral properties of the halos, which can be very uniform to reasonably patchy (Donnert *et al.* 2010a). A great deal of debate on this issue can be found in a series of publications, as summarised in Brunetti & Jones (2014).

The neutral pions generated during the proton–proton collisions are expected to decay as γ-ray emission (Blasi *et al.* 2007), which can be considered as an additional by-product of the hadronic model. It is the γ-ray emission, which gives an additional property to well constrain the secondary model, and the initially considered normalisation of CR protons with power-law spectra. Although with the existing γ-ray telescopes (FERMI telescope), yet no conclusive evidence of γ-ray emission has been observed in clusters, except for the more recent work by Baghmanyan *et al.* (2022) showing some indications of extended emission from the nearby Coma cluster. There is a trade-off in the hadronic model, between the radio halo luminosity and the corresponding γ-ray emissivity if halo emission is purely the cause of secondary particles (CR electrons). Another recent study towards the Coma cluster by Adam *et al.* (2021) reports the detection of gamma-rays, but they find that the hadronic model is insufficient to explain the radio halo.

Although the numerical predictions for secondary electron models for radio halo emission do not favour the current observations of radio halos, it is found to be an effective model to explain the mini-halo radio structures (e.g., Pfrommer & Enßlin 2004a; Ignesti *et al.* 2020). Ignesti *et al.* (2020) consider the hadronic scenario, where they assume the CR-proton injection from the central AGN and CR-proton energy-independent diffusion coefficient, to estimate the CR-proton spectrum to finally arrive at the radio emission profile. In their work, the final electron spectrum is computed assuming stationary conditions (Brunetti *et al.* 2017), which on the first-order approximation can be justified by the cooling time. On this timescale, the CR-protons can diffuse to scales similar to that of mini-halos, within the duty cycles of the AGN. Unfortunately, due to the high complexity of physical processes in the cooling flow clusters, no explicit attempts have been made to numerically simulate such structures.

6.6 *Numerical simulations of magnetic fields in ICM*

Existing studies discussed in Section 3.6 that compare observations of the Faraday RM and depolarisation of cluster radio sources with those derived from numerical models reveal that the magnetic fields in the ICM to be ordered on kpc-scales and have strengths of few μG. Magnetic fields in the ICM can be amplified and

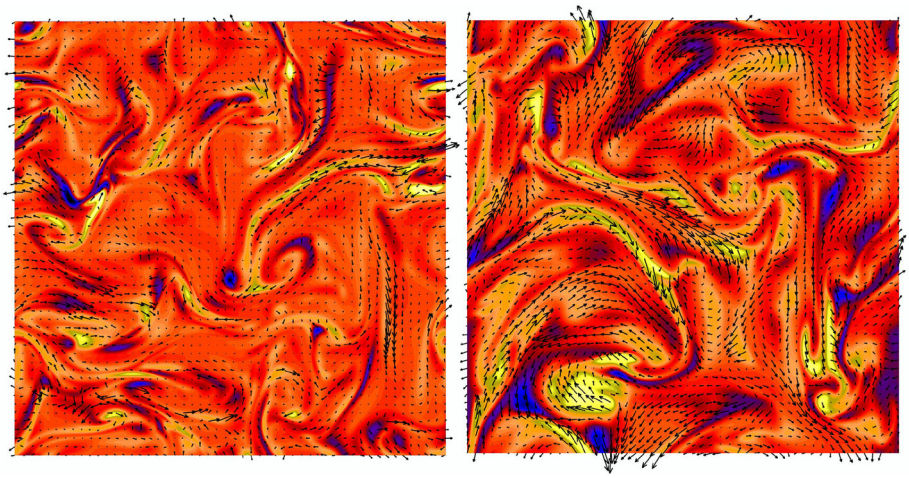

Figure 8. Two-dimensional snapshots capturing the evolution of the magnetic field from initial (left) to the steady state configuration (right), due to fluctuation dynamo action from a run with $\mathcal{M} = 0.18$, Pm $= 1$ and turbulence driven on 256 kpc scales. Here, the z-component of the field is shown in colours in the x–y plane. The fields are strong in blue and yellow regions and negligible in orange regions. The field in the plane of the slices is shown with arrows whose length is proportional to the field strength. See Sur (2019) and Sur *et al.* (2021) for details on the simulation setup and initial conditions.

maintained at equipartition[3] levels via several processes operating on a large range of scales. For example, on several hundreds of kpc scales, shearing motion and sloshing of gas due to off-axis cluster mergers can drive turbulence (Subramanian *et al.* 2006). This turbulence can be driven by the cascade of vortical motions produced in oblique shocks as an aftermath of cluster formation and/or major collisions (Norman & Bryan 1999; Subramanian *et al.* 2006; Ryu *et al.* 2008; Xu *et al.* 2012; Miniati 2015; Marinacci *et al.* 2018). On the other hand, on a few tens of kpc scales, AGN and star-formation driven winds in cluster galaxies can drive turbulence (Donnert *et al.* 2009; Dubois *et al.* 2012; Pakmor *et al.* 2016; Wiener *et al.* 2017).

In the absence of noticeable rotation, fluctuation dynamos are ideally suited to amplify dynamically insignificant seed magnetic fields by randomly stretching them in turbulent eddies (Haugen *et al.* 2004; Schekochihin *et al.* 2004; Federrath *et al.* 2011; Porter *et al.* 2015; Sur *et al.* 2018; Seta & Federrath 2021). Fluctuation dynamos amplify the fields to μG levels and order them on kpc-scales in a fast and efficient way (Kazantsev 1968; Zeldovich *et al.* 1990). The amplification of fields by this mechanism occurs on the eddy-turnover timescale ($\sim 10^8$ yr), which does not require any rotation or density stratification and only relies on the random or turbulent nature of the fluid flow. Figure 8 shows that the resulting structure of the fluctuation dynamo generated magnetic fields from numerical simulations of Sur *et al.* (2021) is intermittent and arranged in folds (also see Seta *et al.* 2020), and are clearly in contrast to Gaussian field distributions (e.g., Murgia *et al.* 2004).

Cosmological simulations of tens of Mpc scales have shed meaningful insights into the role of magnetic fields in structure formation in the Universe (see e.g., Ryu *et al.* 2008; Donnert *et al.* 2009; Miniati 2015; Vazza *et al.* 2009a, 2006, 2021a; Marinacci *et al.* 2018), and in understanding the radial distribution of gas and magnetic fields. Some of these simulations also confirm the possibility of fluctuation dynamo action in galaxy clusters (e.g., Miniati 2015; Marinacci *et al.* 2018; Vazza *et al.* 2006; Domínguez-Fernández *et al.* 2019). Although these simulations are a powerful tool and are complementary to periodic box, local dynamo simulations, the limited resolution achievable to resolve the turbulent scales together with uncontrollable numerical dissipation (due to the use of ideal MHD) may substantially affect the evolution and properties of magnetic fields. In fact, Vazza *et al.* (2006) are able to achieve a resolution ≈3.95 kpc at best by using the adaptive mesh refinement technique. Moreover, cosmological simulations of galaxy cluster assembly and evolution, at present, are only able to follow the dynamical behaviour for only a few tens of dynamical times (due to exorbitant computational costs). This implies that the magnetic energy would

[3]Here, 'equipartition' refers to the energy density of magnetic fields and kinetic energy of gas.

be grossly underestimated, with its value depending on the initial seed field and the effective Reynolds number of the simulation (Beresnyak & Miniati 2016). Until computational power and numerical implementation are sufficient for performing cosmological simulations by aptly capturing the fluctuation dynamo action as well as resolving scales closer to the dissipation scale, numerical simulations of smaller volumes (<1 Mpc^3) with high resolutions, $\mathcal{O}(1$ kpc), can be useful to gain meaning insights on the properties of magnetic fields and their observational signatures (e.g., Subramanian *et al.* 2006; Bhat & Subramanian 2013; Sur 2019).

6.6.1 Polarised emission from fluctuation dynamo action To study the expected properties of the polarised synchrotron emission in the ICM due to the action of fluctuation dynamo, high resolution (1 kpc) simulations of a 512^3 kpc^3 volume, representing the realistic conditions in the core regions of ICM, have been recently analysed by Sur *et al.* (2021) and Basu & Sur (2021) using the COSMIC polarisation transfer package (Basu *et al.* 2019). By including the effects of frequency-dependent Faraday,[4] and frequency-independent beam depolarisation,[5] synthetic 2-D maps of the polarised synchrotron emission in the 0.5–7 GHz range and maps of Faraday depth were investigated for various representative scales of turbulent driving (l_f). In the presence of subsonic turbulence in the ICM, the power spectrum of the Faraday depth map is directly related to the magnetic integral scale ($L_{\mathrm{int},M}$) defined as:

$$L_{\mathrm{int},M} = \frac{2\pi \int [M(k)/k]\, dk}{\int M(k)\, dk}. \quad (6)$$

Here, $M(k)$ is the power spectrum of the magnetic energy and k is the wavenumber. Thus, the power spectrum of the map of Faraday depth can provide insights into the driving scale as it is linearly related to $L_{\mathrm{int},M}$ (Basu & Sur 2021). However, obtaining Faraday depth maps for ICM is tricky due to the faintness of the polarised emission and limitations in analysis techniques, e.g., RM-synthesis (see e.g., Basu *et al.* 2019; Sur *et al.* 2021).

Figure 9 shows the maps of the total synchrotron intensity for different l_f from Basu & Sur (2021). The top panels are at the native 1 kpc resolution of the simulations, and the bottom panels are after smoothing by a telescope beam with FWHM of 30 kpc corresponding to an angular resolution of 10 arcsec at redshift ∼0.2. It is clear that the filamentary structures on small scales are mostly smeared out in the presence of a telescope beam. These studies further revealed that at $\nu \lesssim 1.5$ GHz, a combination of low sensitivity and observation noise results in polarised emission from bright filamentary structures, wherever detectable, to be confined as clumps that could originate either due to shock compression or from Faraday depolarisation.

Moreover, at low frequencies ($\nu \lesssim 1.5$ GHz), telescope beam drastically affects the properties of polarised emission in the presence of Faraday rotation (shown in the bottom panels of Figure 9). Thus, such detection may not provide adequate information on the global properties of turbulent magnetic fields in the ICM. On the other hand, the effects of Faraday depolarisation and beam smoothing are mitigated for $\nu \gtrsim 4$ GHz with polarisation remaining largely unaffected and the mean fractional polarisation ($\langle p \rangle$) follows the $\langle p \rangle \propto l_f^{1/2}$ relation as expected from random walk of the polarisation vector when averaged over a volume (Basu & Sur 2021).

This indicates that observational estimates of, or constrain on, $\langle p \rangle$ at $\nu \gtrsim 4$ GHz could be effectively used as an indicator of the driving scale of turbulence in the ICM, strongly underlining the need for high-frequency ($\gtrsim$4 GHz) polarisation observations of radio halos using current or future radio telescopes. As $\langle p \rangle$ depends on l_f above ∼4 GHz, for observations performed with a spatial resolution better than ∼30 kpc (i.e., angular resolution of ∼10 arcsec for a cluster at $z \sim 0.2$), $l_f \lesssim 20$ kpc gives rise to $\langle p \rangle \lesssim 0.05$ indicating turbulence driven by gas accretion and star formation feedback from galaxies, $\langle p \rangle$ in the range 0.05–0.2 would arise for l_f in the range of 20–100 kpc driven by AGN feedback, while for $l_f \gtrsim 150$ kpc, $\langle p \rangle \gtrsim 0.2$ is expected, indicating turbulence being driven via vortical motions from cluster mergers. Therefore, to effectively probe the properties of polarised emission in the ICM and distinguish the different drivers of turbulence, sensitivity to $\langle p \rangle \gtrsim 0.05$ for total intensity surface brightness ∼2–6 μ Jy beam^{-1} at ∼6–10 arcsec angular resolution is necessary (see Basu & Sur 2021). Future observations with the SKA in band 5a, covering the 4.6–8.5 GHz range, will play a crucial role in the quest of directly unravelling the magnetic field strength and structure in the ICM through polarised emission.

[4] A frequency-dependent reduction in polarisation wherein emission originating from different locations along the line of sight undergo different degrees of Faraday rotation in the thermal component of the ICM gas.

[5] A reduction in the polarisation caused by cancellation due to turbulent magnetic fields on scales smaller than the telescope beam.

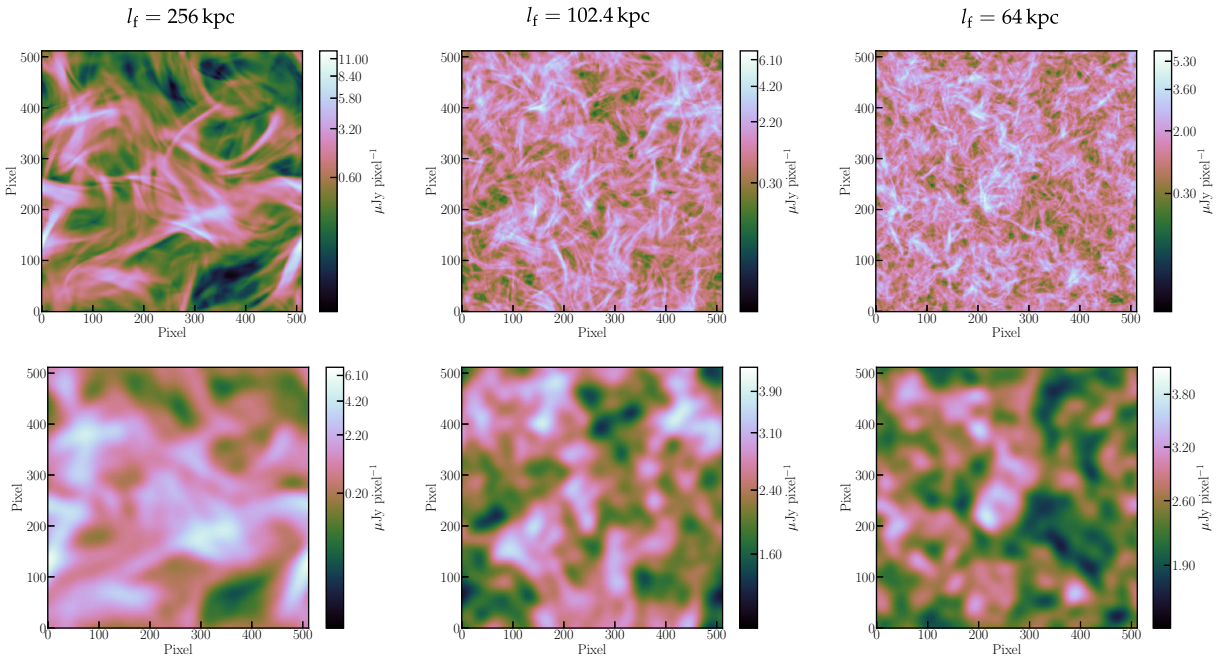

Figure 9. Effect of turbulent driving: The top row shows 2D maps of the surface brightness of the total synchrotron emission at the native resolution of the simulations. The bottom row shows the same maps when smoothed on 30 kpc scales. These figures are from Sur *et al.* (2021) and Basu & Sur (2021).

6.7 *Modelling mechanical heating by AGN*

There is a pool of growing evidence, from both observations and simulations, that heating by the central AGN plays a role in the evolution of galaxy clusters and hence, in the formation of the large-scale structural formation (Nath & Roychowdhury 2002; Roychowdhury *et al.* 2005; Guo & Oh 2008; Gaspari *et al.* 2011; Chaudhuri *et al.* 2012, 2013; Prasad *et al.* 2015; Iqbal *et al.* 2017a). This idea gets support from the fact that about 70% of galaxy clusters host central AGN. The ultra-steep spectrum radio bubbles (AGN remnants) in X-ray detected cavities found in the ICM is a direct proof of AGN energy being injected into ICM. Moreover, the mechanical power of the radio jets is found to be much larger than the synchrotron power (Cavagnolo *et al.* 2010; Godfrey & Shabala 2013), implying even weak radio sources could produce enough mechanical power to significantly affect the ICM properties up to large radii and prevent gas from cooling. The feedback physics is driven by non-thermal electrons, directly or indirectly, and hence, diffuse radio emissions in clusters are correlated to feedback mechanisms.

By comparing the observed entropy profiles with theoretically expected entropy profiles, based on non-radiative simulations, Chaudhuri *et al.* (2012, 2013) and Iqbal *et al.* (2017b) were able to estimate the energy deposition profiles in the ICM. Chaudhuri *et al.* (2013) found an excess mean energy per particle to be around ∼1.6–2.7 keV up to r_{500}. Using the NRAO/VLA Sky Survey source catalogue, Chaudhuri *et al.* (2013) found that the total radio luminosity at 1.4 GHz of the central source(s) correlates with feedback energy, albeit with different normalisation for cool-core and non-cool-core clusters. Iqbal *et al.* (2017a, b) estimated energy deposition profiles in galaxy clusters up to the cluster virial radius. Their results conclusively rule out any pre-heating of the ICM, but agreed with the earlier findings of Chaudhuri *et al.* (2013). In another work, Iqbal *et al.* (2018) using Chandra X-ray and VLA/GMRT radio data in the cluster inner regions found a significant correlation between the BCG radio luminosity (L_R) and cluster bulk properties. In the left panel in Figure 10, we show the median non-gravitational feedback energy as a function of radius for the ACCEPT Cavagnolo *et al.* (2009) sub-sample and the REXCESS Böhringer *et al.* (2007); Pratt *et al.* (2010) sample, as estimated in Iqbal *et al.* (2018). The profiles are centrally peaked and decrease with radius. The right panel, in Figure 10, shows the correlation between the BCG radio luminosity and X-ray luminosity as estimated in Iqbal *et al.* (2018). These results suggest that AGN play a dominant role in heating the ICM and that also AGN feedback is intricately linked with cluster radio emission.

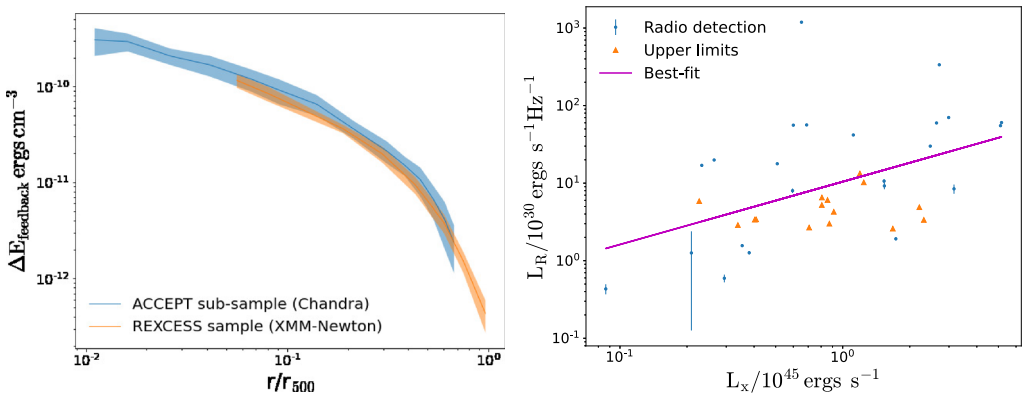

Figure 10. Left panel: Feedback energy per unit volume in the ACCEPT sub-sample (Iqbal *et al.* 2018) and the REXCESS sample (Chaudhuri *et al.* 2013). Right panel: Correlation between BCG-radio luminosity and X-ray luminosity in the ACCEPT sub-sample (Iqbal *et al.* 2018).

There are currently three main AGN feedback mechanisms (models) which can be explored without resorting to complex hydro-dynamical simulations: (i) the acoustic model (Fabian *et al.* 2003, 2005), (ii) the effervescent model (Ruszkowski & Begelman 2002; Roychowdhury *et al.* 2004) and (iii) the cosmic-ray model (Guo & Oh 2008; Fujita & Ohira 2011). In the acoustic model, the dissipation of energy into the ICM is due to sound waves induced by the central AGN activity, while in the effervescent model, the AGN injects non-thermal electrons filled buoyant bubbles into the ICM, which then heat the ambient medium by doing pdV work. The CR model assumes that cosmic rays are injected by the AGN, which can then heat the cluster core by amplifying Alfvén waves (Guo & Oh 2008; Fujita & Ohira 2011). Although all the models assume the central AGN to be the main source of feedback energy, they are radically different with regard to the physics of dissipation of energy into the ICM. All the three models, in principle, can be constrained by studying the mechanical jet power and radio luminosity ($L_{\rm jet}$–$L_{\rm R}$) scaling relations (Cavagnolo *et al.* 2010; Godfrey & Shabala 2013) and the thermal properties of the ICM using X-rays and radio measurements. Unfortunately, with current X-ray and radio observations, it is not possible to differentiate unambiguously between these models (Iqbal *et al.* 2022). However, upcoming high-quality data from large surveys with uGMRT and SKA (in radio), CMB-S4 (in mm) and Athena (in X-rays) will provide us new insights on AGN feedback of the ICM up to $z \sim 2$.

7. Updated taxonomy of cluster radio sources

As discussed earlier in Section 3.1, historically, the cluster radio sources were classified broadly into radio halos, relics and mini-halos mostly based on their physical characteristics (Enßlin *et al.* 1998; Giovannini *et al.* 1999; Feretti & Giovannini 2008; Feretti *et al.* 2012). However, with the improved sensitivity and wide spectral coverage of telescopes in recent years, a variety of extended low-brightness features have been commonly detected in clusters, slowly blurring the lines between radio galaxies and diffuse cluster radio sources. Many of these sources are morphologically similar to well known cluster radio sources, but sharply differing in their spectral properties, especially in steepness and curvature. This has necessitated the inclusion of revived AGN fossil plasma sources, phoenices and GReET together as a new class of cluster radio sources, making the overall classification scheme a very complex one (van Weeren *et al.* 2019), a mixture of multiple parameters such as location, morphology, spectra, etc.

Nevertheless, it is evident that in general, radio halos, mini-halos and peripheral relics are detected with a power-law spectrum, AGN relics or fossil plasma sources, phoenices, etc. exhibit a curved spectrum. As per our current understanding and the suggested theoretical models (see Section 6), while the power-law spectrum favours an *in-situ* particle acceleration mechanism, spectral curvature due to the ageing of electrons indicates the dying or revival of synchrotron emitting electrons. Therefore, the major factors that determine the energy distribution and the appearance, are the initial electron energy spectrum (steepness) and the dynamics of the cluster medium that drives the particle (re-)acceleration engines.

Since a substantial number of cluster radio sources are now available with their spectral information in wider frequency bands and the list is only expected to grow in future, we propose here a novel idea for classifying these sources based on their origin, specifically

on the type of source (injection) electrons and cluster dynamics. This would in future help us to rationalize the classification and the nomenclature of a large variety of diffuse radio sources being observed. In this proposed taxonomy, we call a type of source as (i) active cluster radio source if the sources show a power-law spectrum with no obvious spectral curvature. Since the power-law spectrum is the characteristics of freshly accelerated non-thermal particles, it indicates the presence of *in-situ* and active particle acceleration engines in these sources, such as usual radio-halos, relics and mini-halos. The sources will be called as the (ii) dying cluster radio sources, if they are of ultra-steep spectrum nature with spectral curvature and age $\lesssim$100 Myr with no obvious particle acceleration engine found in the system. AGN relics, ultra-steep radio halos with spectral curvature, etc., would fall in this group. And a third one is defined as the (iii) revived cluster radio sources, in case the emission comes from the revival of fossil non-thermal electrons, where cluster shock or turbulence is involved. However, they act as the revival engine rather than an accelerating engine and keep the curved spectrum nature of the injected fossil or aged electrons, intact. The basic feature of these sources are an ultra-steep spectrum, spectral curvature and a spectral age of usually beyond 100 Myr, such as radio phoenices, revived ultra-steep sources by turbulence, revived buoyant radio bubbles, etc.

While the existing classification scheme would remain relevant for immediate categorisation of the overall cluster radio sources, our proposed taxonomy would help in classifying them further into more fundamental level. Such a classification would not be host-specific, rather would be applicable to a wider variety of radio emissions in various large scale structures. However, it should be noted that the classification always evolve in time with the availability of more data and as our understanding of the systems progressively improves.

8. Role of uGMRT and expectations with the SKA

For a complete understanding of physics of the ICM and the interplay between the galaxies and ICM, it is going to be important to make deep continuum observations, in particular, focussing on polarisation and spectral line studies, of these components across a wide range of frequency bands. Recent galaxy cluster surveys, such as LoTSS at 144 MHz and MGCLS at 1283 MHz (Section 2) have resulted in numerous discoveries of diffuse radio emission from galaxy clusters. The uGMRT, given its full coverage of the LOFAR sky, in addition to a significant overlap with the MeerKAT sky, is well suited for providing follow-up observations, in the frequency range of 150–1400 MHz, for obtaining spectra of such diffuse radio sources. Polarisation studies at sub-GHz frequencies are challenging, but will be of interest to study sources that have ultra-steep spectra. The uGMRT bands 3 and 4 are being tested to make polarisation measurements (Silpa *et al.* 2021) and will be of interest to study magnetic fields in sources, such as radio relics and phoenices.

The μJy level sensitivity that the SKA will achieve, will transform our understanding of the statistical properties of large scale structures, like galaxy clusters down to 10^{14} $M_{\odot}$ and beyond $z \geq 1$. This has been limited until now due to the sensitivity and resolution constraints imposed by current generation instruments (Cassano *et al.* 2015). It will also help us to probe the distant Universe via cluster gravitational lensing, particularly at radio wavelengths, where the number of known radio-emitting lensed galaxies (a few mJy, up to μJy level) are scarce from $z \geq 1$ (McKean *et al.* 2015, Section 2.1.8 by Pandey-Pommier *et al.* in Acero *et al.* 2017 and Pandey-Pommier *et al.* SKA Users case, Pvt. communication).

Deep continuum imaging of galaxies belonging to clusters is also necessary to study the effect of ICM on galaxies and vice versa. SKA continuum surveys will provide unprecedented sensitivities to study cluster fields in depth. Continuum imaging at 0.2–0.6 arcsec, and 3 μJy per beam sensitivity on clusters along with spectral line (HI) surveys of lensed galaxies at SKA-Low (0.05–0.35 GHz), SKA1-Mid band 1 (0.35–1.05) and 2 (0.95–1.76) frequencies will not only help to discover the intra-cluster filaments at lower redshifts $z \leq 0.1$ and investigate the matter distribution within clusters up to $z \sim 1$, but also may discover a new population of background star-forming galaxies up to ($0 \leq z \leq 6$) via imaging. Further, for higher redshift lensed galaxies, ($z \leq 5$) continuum imaging and spectral line observations, in band 5 (4.6–15.3 GHz) with 0.05–0.1 arcsec and 0.3 μJy level sensitivity, will provide insights into the cold molecular gas reservoirs (CO, HCN, HCO^{+}, etc.) (Carilli & Walter 2013) that trace the sites of ongoing star formation. Additionally, the deep HI and continuum imaging provided with the uGMRT in band 5 (1.4 GHz) with 2.5 μJy per beam sensitivity and 2.3 arcsec resolution will help us trace the impact of the extreme cluster environment on the atomic gas (HI) reservoirs, and also disentangle the HI

emission from the cluster central regions and the filaments (Pandey-Pommier *et al.* SKA users case, Pvt. communication).

9. Summary and conclusions

Radio observations of galaxy clusters are direct probes of a variety of phenomena on scales ranging from galaxies to the large scale structures. Diffuse radio sources found in galaxy clusters represent signatures of synchrotron emission delineating the magnetic fields in a cluster-scale system, along with the presence of relativistic electrons in the ICM. These sources have low surface brightness ($\sim\mu$Jy arcsec^{-2} at GHz), steep spectra ($\alpha < -1$ with $S_\nu \propto \nu^\alpha$) and extend up to several tens of arcminutes (in low redshift sources). Thus, low frequency telescopes with good sensitivity to extended structures with low rms noise, are essential for these studies.

In this work, we have reviewed the current understanding of this field using current radio observations, along with theoretical models and simulations, and outline the priorities for upcoming and already operational radio telescopes. We summarise as follows:

1. The detailed scientific study of physical phenomena in galaxy groups and clusters require radio observations with high resolution (reaching sub-kpc scales) and with good sensitivity to extended structures (few arcminutes to a degree). Thus, large telescopes such as the VLA, WSRT and GMRT have played an important role in the past several decades in these studies. The upgraded GMRT, LOFAR and MeerKAT have recently become operational, and are providing new insights on the physics of the galaxy clusters and beyond. The SKA is a next generation radio telescope, which will further revolutionise the field.
2. Radio surveys targeting galaxy clusters in the past two decades have thrown light on the statistics of occurrence of diffuse radio emission in clusters. Currently, several all-sky surveys, such as those with the LOFAR, are regularly generating numerous new discoveries that need detailed follow-up to uncover their nature and origin.
3. Diffuse radio emission from clusters of galaxies is broadly classified into radio halos, relics and mini-halos. There are other diffuse filamentary extended radio sources found in galaxy clusters that result from activities or mergers of radio galaxies. The interaction between the cluster ICM and the radio sources can lead to radio sources being revived. Radio phoenices, turbulence-revived sources and buoyant radio bubbles are sources in this category.
4. The focus of radio surveys is shifting to low mass clusters and groups where the state of the magnetic field and extent of the generation of cosmic rays is poorly known.
5. At the other extreme of spatial extent, superclusters of galaxies which can stretch beyond 10–100 Mpc belong to a scale, where the origin and nature of magnetic fields are poorly known. The detection of synchrotron-emitting radio bridges between pairs of clusters indicate that substantial magnetic fields do exist on such scales, and the dense environment of superclusters may host large scale radio sources that can provide the direct detection of such magnetic fields. Currently, both superclusters and binary clusters are being surveyed in the radio bands.
6. Theoretical models have proposed mechanisms that explain the origin and nature of diffuse radio sources to a large extent, though there are unsolved challenges. The DSA model falls short of explaining the observed radio relics unless the seed relativistic electron population is included. Several variants of the turbulent reacceleration model, such as using compressible and incompressible turbulence, Alfvén modes and fast modes, have been proposed for explaining radio halos. Efforts are ongoing to numerically solve the Fokker–Planck equation to follow the reacceleration of every particle in a typical simulation box. However, overcoming numerical limitations and obtaining predictions specific to a variety of merger scenarios will be needed.
7. Recent numerical simulations of magnetic fields show intermittent morphological signatures, arranged in folds, in contrast to Gaussian field distributions that are typically considered in the literature. Cosmological simulations are reaching unprecedented resolution scales (current down to a few kpc), though more needs to be done to capture the fluctuation dynamo and resolution scales of the order of dissipation scales. Simulations of observations show that polarisation observations at 4 GHz and above could potentially be used to find the driving scales of turbulence.
8. By studying the radio sources in the central galaxies in clusters and groups, constraints can be obtained on the mechanical heating of the cluster cores by AGN. This will lead to the understanding of the physics of the interaction of the thermal and

non-thermal plasma in the ICM, and the accretion processes associated with the supermassive black holes at the cores of the brightest cluster and group galaxies.

9. The upgraded GMRT with its wide frequency coverage will play a major role as a follow-up instrument for the newly discovered radio sources with LOFAR and MeerKAT, paving the way for SKA.
10. With the advent of SKA, significant progress in understanding the open issues regarding the origin and nature of magnetic fields and cosmic rays on the scales of clusters and beyond is expected.

Acknowledgements

Paul wants to thank the DST INSPIRE faculty scheme (code: IF-12/PH-44) for funding his research group. Kale acknowledges the support of the Department of Atomic Energy, Government of India, under project no. 12-R&D-TFR-5.02-0700. Sur acknowledges computing time awarded the CDAC National Param supercomputing facility, India, under the grant 'Hydromagnetic-Turbulence-PR' and the use of the High Performance Computing (HPC) resources made available by the Computer Centre of the Indian Institute of Astrophysics. Sur further thanks the Science and Engineering Research Board (SERB) of the Department of Science & Technology (DST), Government of India, for support through research grant ECR/2017/001535. Basu acknowledges the computing facility and support provided at the Thüringer Landessternwarte, Tautenburg, Germany. The work of Iqbal was supported by CNES, France. MP acknowledges the support of CEFIPRA foundation under the project 6504-3. MR acknowledges financial support from Ministry of Science and Technology of Taiwan (MOST 109-2112-M-007-037-MY3).

References

Acero F., Acquaviva J. T., Adam R., *et al.* 2017, arXiv e-prints, 1712.06950
Adam R., Goksu H., Brown S., Rudnick L., Ferrari C. 2021, A&A, 648, A60
Akamatsu H., Kawahara H. 2013, PASJ, 65, 16
Araya-Melo P. A., Aragón-Calvo M. A., Brüggen M., Hoeft M. 2012, MNRAS, 423, 2325
Bagchi J., Enßlin T. A., Miniati F., *et al.* 2002, Nature, 7, 249
Bagchi J., Sankhyayan S., Sarkar P., *et al.* 2017, ApJ, 844, 25
Bagchi J., Sirothia S. K., Werner N., *et al.* 2011, ApJL, 736, L8
Baghmanyan V., Zargaryan D., Aharonian F., *et al.* 2022, MNRAS, 516, 562
Bahcall N. A., Soneira R. M. 1984, ApJ, 277, 27
Basu A., Fletcher A., Mao S. A., *et al.* 2019, Galaxies, 7, 89
Basu A., Sur S. 2021, Galaxies, 9, 62
Basu K. 2012, MNRAS, 421, L112
Basu K., Erler J., Sommer M., Vazza F., Eckert D. 2016a, Galaxies, 4, 73
Basu K., Vazza F., Erler J., Sommer M. 2016b, A&A, 591, A142
Beresnyak A., Miniati F. 2016, ApJ, 817, 127
Bhat P., Subramanian K. 2013, MNRAS, 429, 2469
Bhatnagar S., Cornwell T. J., Golap K., Uson J. M. 2008, A&A, 487, 419
Biava N., Brienza M., Bonafede A., *et al.* 2021, A&A, 650, A170
Birkinshaw M. 1999, Phys. Rep., 310, 97
Bîrzan L., Rafferty D. A., Brüggen M., *et al.* 2020, MNRAS, 496, 2613
Blandford R., Eichler D. 1987, Phys. Rep., 154, 1
Blanton E. L. 2004, in The Riddle of Cooling Flows in Galaxies and Clusters of galaxies, eds Reiprich T., Kempner J., Soker N., p. 181
Blasi P., Colafrancesco S. 1999, Nuclear Physics B Proceedings Supplements, 70, 495
Blasi P., Gabici S., Brunetti G. 2007, International Journal of Modern Physics A, 22, 681
Blundell K. M., Fabian A. C., Crawford C. S., Erlund M. C., Celotti A. 2006, ApJL, 644, L13
Böhringer H., Chon G., Kronberg P. P. 2016, A&A, 596, A22
Böhringer H., Schuecker P., Pratt G. W., *et al.* 2007, A&A, 469, 363
Bonafede A., Feretti L., Govoni F., *et al.* 2009a, in Revista Mexicana de Astronomia y Astrofisica Conference Series, Vol. 36, Revista Mexicana de Astronomia y Astrofisica Conference Series, CD303–CD307
Bonafede A., Feretti L., Giovannini G., *et al.* 2009b, A&A, 503, 707
Bonafede A., Feretti L., Murgia M., *et al.* 2010, A&A, 513, A30
Bonafede A., Intema H., Brüggen M., *et al.* 2015, MNRAS, 454, 3391
Bonafede A., Cassano R., Brüggen M., *et al.* 2017, MNRAS, 470, 3465
Botteon A., Brunetti G., Ryu D., Roh S. 2020a, A&A, 634, A64
Botteon A., Gastaldello F., Brunetti G., Dallacasa D. 2016, MNRAS, 460, L84
Botteon A., Shimwell T., Bonafede A., *et al.* 2018, MNRAS, 478, 885
Botteon A., Cassano R., Eckert D., *et al.* 2019, A&A, 630, A77
Botteon A., van Weeren R. J., Brunetti G., *et al.* 2020b, MNRAS, 499, L11

Botteon A., Cassano R., van Weeren R. J., *et al.* 2021, ApJL, 914, L29
Botteon A., Shimwell T. W., Cassano R., *et al.* 2022, A&A, 660, A78
Braun R., Bonaldi A., Bourke T., Keane E., Wagg J. 2019, arXiv e-prints, 1912.12699
Bravi L., Gitti M., Brunetti G. 2016, MNRAS, 455, L41
Breen J., Raychaudhury S., Forman W., Jones C. 1994, ApJ, 424, 59
Brienza M., Godfrey L., Morganti R., *et al.* 2016, A&A, 585, A29
Brienza M., Shimwell T. W., de Gasperin F., *et al.* 2021, Nature Astronomy, 5, 1261
Brienza M., Lovisari L., Rajpurohit K., *et al.* 2022, A&A, 661, A92
Brüggen M., Vazza F. 2020, MNRAS, 493, 2306
Brüggen M., Rafferty D., Bonafede A., *et al.* 2018, MNRAS, 477, 3461
Brunetti G., Blasi P. 2005, MNRAS, 363, 1173
Brunetti G., Blasi P., Cassano R., Gabici S. 2004, MNRAS, 350, 1174
Brunetti G., Jones T. W. 2014, International Journal of Modern Physics D, 23, 1430007
Brunetti G., Lazarian A. 2007, MNRAS, 378, 245
Brunetti G., Lazarian A. 2011a, MNRAS, 410, 127
Brunetti G., Lazarian A. 2011b, MNRAS, 412, 817
Brunetti G., Vazza F. 2020, Physical Review Letters, 124, 051101
Brunetti G., Zimmer S., Zandanel F. 2017, MNRAS, 472, 1506
Buote D. A. 2001, ApJL, 553, L15
Burns J. O., Hanisch R. J., White R. A., *et al.* 1987, AJ, 94, 587
Carilli C. L., Walter F. 2013, ARAA, 51, 105
Cassano R., Brunetti G., Setti G., Govoni F., Dolag K. 2007, MNRAS, 378, 1565
Cassano R., Ettori S., Giacintucci S., *et al.* 2010, ApJL, 721, L82
Cassano R., Ettori S., Brunetti G., *et al.* 2013, ApJ, 777, 141
Cassano R., Bernardi G., Brunetti G., *et al.* 2015, in Advancing Astrophysics with the Square Kilometre Array (AASKA14), 73
Cautun M., van de Weygaert R., Jones B. J. T., Frenk C. S. 2014, MNRAS, 441, 2923
Cavagnolo K. W., Donahue M., Voit G. M., Sun M. 2009, ApJS, 182, 12
Cavagnolo K. W., McNamara B. R., Nulsen P. E. J., *et al.* 2010, ApJ, 720, 1066
Cen R., Ostriker J. P. 1999, ApJ, 514, 1
Chatterjee S., Rahaman M., Datta A., Raja R. 2022, AJ, 164, 83
Chaudhuri A., Majumdar S., Nath B. B. 2013, ApJ, 776, 84
Chaudhuri A., Nath B. B., Majumdar S. 2012, ApJ, 759, 87
Churazov E., Ruszkowski M., Schekochihin A. 2013, MNRAS, 436, 526
Churazov E., Sunyaev R., Forman W., Böhringer H. 2002, MNRAS, 332, 729
Clarke T. E., Kronberg P. P., Böhringer H. 2001, ApJL, 547, L111
Clarke T. E., Sarazin C. L., Blanton E. L., Neumann D. M., Kassim N. E. 2005, ApJ, 625, 748
Colafrancesco S., Marchegiani P., Palladino E. 2003, A&A, 397, 27
Cornwell T. J., Golap K., Bhatnagar S. 2008, IEEE Journal of Selected Topics in Signal Processing, 2, 647
Cuciti V., Brunetti G., van Weeren R., *et al.* 2018, A&A, 609, A61
Cuciti V., Cassano R., Brunetti G., *et al.* 2021a, A&A, 647, A51
Cuciti V., Cassano R., Brunetti G., *et al.* 2021b, A&A, 647, A50
da Costa L. N., Numes M. A., Pellegrini P. S., *et al.* 1986, AJ, 91, 6
David L. P., Jones C., Forman W., *et al.* 2009, ApJ, 705, 624
Day C. S. R., Fabian A. C., Edge A. C., Raychaudhury S. 1991, MNRAS, 252, 394
de Gasperin F., van Weeren R. J., Brüggen M., *et al.* 2014, MNRAS, 444, 3130
de Gasperin F., Intema H. T., Shimwell T. W., *et al.* 2017a, Science Advances, 3, e1701634
de Gasperin F., Intema H. T., Ridl J., *et al.* 2017b, A&A, 597, A15
de Gasperin F., Rudnick L., Finoguenov A., *et al.* 2022, A&A, 659, A146
de Graaff A., Cai Y.-C., Heymans C., Peacock J. A. 2019, A&A, 624, A48
de Lapparent V., Geller M. J., Huchra J. P. 1988, ApJ, 332, 44
Dennison B. 1980, ApJL, 239, L93
Deo D. K., Kale R. 2017, Experimental Astronomy, 44, 165
Di Gennaro G., van Weeren R. J., Cassano R., *et al.* 2021a, A&A, 654, A166
Di Gennaro G., van Weeren R. J., Brunetti G., *et al.* 2021b, Nature Astronomy, 5, 268
Dolag K., Enßlin T. A. 2000, A&A, 362, 151
Dominguez-Fernandez P., Bruggen M., Vazza F., *et al.* 2021, MNRAS, 500, 795
Domínguez-Fernández P., Vazza F., Brüggen M., Brunetti G. 2019, MNRAS, 486, 623
Dong R., Stone J. M. 2009, ApJ, 704, 1309
Donnert J., Brunetti G. 2014, MNRAS, 443, 3564
Donnert J., Dolag K., Brunetti G., Cassano R. 2013, MNRAS, 429, 3564
Donnert J., Dolag K., Brunetti G., Cassano R., Bonafede A. 2010a, MNRAS, 401, 47
Donnert J., Dolag K., Cassano R., Brunetti G. 2010b, MNRAS, 407, 1565
Donnert J., Dolag K., Lesch H., Müller E. 2009, MNRAS, 392, 1008
Drury L. O. 1983, Reports on Progress in Physics, 46, 973

Dubois Y., Devriendt J., Slyz A., Teyssier R. 2012, MNRAS, 420, 2662
Duchesne S. W., Johnston-Hollitt M., Bartalucci I. 2021, PASA, 38, e053
Duchesne S. W., Johnston-Hollitt M., Riseley C. J., Bartalucci I., Keel S. R. 2022, MNRAS, 511, 3525
Dwarakanath K. S., Kale R. 2009, ApJL, 698, L163
Dwarakanath K. S., Parekh V., Kale R., George L. T. 2018, MNRAS, 477, 957
Eckert D., Jauzac M., Vazza F., *et al.* 2016, MNRAS, 461, 1302
Enßlin T., Pfrommer C., Miniati F., Subramanian K. 2011, A&A, 527, A99
Enßlin T. A., Biermann P. L., Klein U., Kohle S. 1998, A&A, 332, 395
Enßlin T. A., Brüggen M. 2002, MNRAS, 331, 1011
Enßlin T. A., Gopal-Krishna. 2001, A&A, 366, 26
Fabian A. C., Celotti A., Blundell K. M., Kassim N. E., Perley R. A. 2002, MNRAS, 331, 369
Fabian A. C., Reynolds C. S., Taylor G. B., Dunn R. J. H. 2005, MNRAS, 363, 891
Fabian A. C., Sanders J. S., Allen S. W., *et al.* 2003, MNRAS, 344, L43
Fabian A. C., Sanders J. S., Ettori S., *et al.* 2000, MNRAS, 318, L65
Fang K., Linden T. 2016, JCAP, 2016, 004
Federrath C., Chabrier G., Schober J., *et al.* 2011, Physical Review Letters, 107, 114504
Federrath C., Klessen R. S., Iapichino L., Beattie J. R. 2021, Nature Astronomy, 5, 365
Federrath C., Klessen R. S., Schmidt W. 2008, ApJL, 688, L79
Feretti L., Giovannini G. 2008, in A Pan-Chromatic View of Clusters of Galaxies and the Large-Scale Structure, eds Plionis M., López-Cruz O., Hughes D., Vol. 740, p. 24
Feretti L., Giovannini G., Govoni F., Murgia M. 2012, A&AR, 20, 54
Ferrari C., Govoni F., Schindler S., Bykov A. M., Rephaeli Y. 2008, SSR, 134, 93
Freeland E., Wilcots E. 2011, ApJ, 738, 145
Fujita Y., Ohira Y. 2011, ApJ, 738, 182
Fujita Y., Takizawa M., Sarazin C. L. 2003, ApJ, 584, 190
Fujita Y., Tawa N., Hayashida K., *et al.* 2008, PASJ, 60, S343
Gardini A. 2007, A&A, 464, 143
Gaspari M., Brighenti F., D'Ercole A., Melioli C. 2011, MNRAS, 415, 1549
Ghirardini V., Bulbul E., Hoang D. N., *et al.* 2021, A&A, 647, A4
Giacintucci S., Markevitch M., Cassano R., *et al.* 2017, ApJ, 841, 71
Giacintucci S., Markevitch M., Venturi T., *et al.* 2014, ApJ, 781, 9
Giacintucci S., O'Sullivan E., Vrtilek J., *et al.* 2011, ApJ, 732, 95
Giacintucci S., O'Sullivan E., Clarke T. E., *et al.* 2012, ApJ, 755, 172
Gilmour R., Best P., Almaini O. 2009, MNRAS, 392, 1509
Giovannini G., Bonafede A., Feretti L., *et al.* 2009, A&A, 507, 1257
Giovannini G., Feretti L. 2000, Nature, 5, 335
Giovannini G., Tordi M., Feretti L. 1999, Nature, 4, 141
Girardi M., Boschin W., Gastaldello F., *et al.* 2016, MNRAS, 456, 2829
Gitti M., Brunetti G., Cassano R., Ettori S. 2018, A&A, 617, A11
Gitti M., O'Sullivan E., Giacintucci S., *et al.* 2010, ApJ, 714, 758
Godfrey L. E. H., Shabala S. S. 2013, ApJ, 767, 12
Govoni F., Murgia M., Feretti L., *et al.* 2005, A&A, 430, L5
Govoni F., Murgia M., Xu H., *et al.* 2013, A&A, 554, A102
Govoni F., Orrù E., Bonafede A., *et al.* 2019, Science, 364, 981
Guo F., Oh S. P. 2008, MNRAS, 384, 251
Gupta Y., Ajithkumar B., Kale H. S., *et al.* 2017, Current Science, 113, 707
Haugen N. E., Brandenburg A., Dobler W. 2004, PRE, 70, 016308
Heinz S., Choi Y.-Y., Reynolds C. S., Begelman M. C. 2002, ApJL, 569, L79
Hoang D. N., Shimwell T. W., Stroe A., *et al.* 2017, MNRAS, 471, 1107
Hoang D. N., Shimwell T. W., van Weeren R. J., *et al.* 2019, A&A, 622, A21
Hoang D. N., Brüggen M., Botteon A., *et al.* 2022, A&A, 665, A60. https://doi.org/10.1051/0004-6361/202243105
Hodgson T., Bartalucci I., Johnston-Hollitt M., *et al.* 2021, ApJ, 909, 198
Hoeft M., Brüggen M. 2007, MNRAS, 375, 77
Hoeft M., Brüggen M., Yepes G., Gottlöber S., Schwope A. 2008, MNRAS, 391, 1511
Hoeft M., Nuza S. E., Gottlöber S., *et al.* 2011, JoAA, 32, 509
Hofmann F., Sanders J. S., Clerc N., *et al.* 2017, A&A, 606, A118
Iapichino L. 2011, MEMSAI, 82, 605
Iapichino L., Maier A., Schmidt W., Niemeyer J. C. 2010, in American Institute of Physics Conference Series, Vol. 1241, Invisible Universe, eds Alimi J.-M., Fuözfa A., p. 928
Ignesti A., Brunetti G., Gitti M., Giacintucci S. 2020, A&A, 640, A37
Intema H. T., Jagannathan P., Mooley K. P., Frail D. A. 2017, A&A, 598, A78
Intema H. T., van der Tol S., Cotton W. D., *et al.* 2009, A&A, 501, 1185
Iqbal A., Kale R., Nath B. B., Majumdar S. 2018, MNRAS, 480, L68
Iqbal A., Majumdar S., Nath B. B., *et al.* 2017a, MNRAS, 472, 713
Iqbal A., Majumdar S., Nath B. B., *et al.* 2017b, MNRAS, 465, L99

Iqbal A., Majumdar S., Nath B. B., Roychowdhury S. 2023, MNRAS, 518, 2735. https://doi.org/10.1093/mnras/stac3197
John R. S., Paul S., Iapichino L., Mannheim K., Kumar H. 2019, MNRAS, 488, 1301
Jones F. C., Ellison D. C. 1991, SSR, 58, 259
Józsa G. I. G., White S. V., Thorat K., *et al.* 2020, in Astronomical Society of the Pacific Conference Series, Vol. 527, Astronomical Data Analysis Software and Systems XXIX, eds Pizzo R., Deul E. R., Mol J. D., de Plaa J., Verkouter H., p. 635
Kaiser N. 1986, MNRAS, 222, 323
Kale R., Dwarakanath K. S. 2012, ApJ, 744, 46
Kale R., Dwarakanath K. S., Bagchi J., Paul S. 2012, MNRAS, 426, 1204
Kale R., Ishwara-Chandra C. H. 2021, Experimental Astronomy, 51, 95
Kale R., Parekh V., Dwarakanath K. S. 2018, MNRAS, 480, 5352
Kale R., Shende K. M., Parekh V. 2019, MNRAS, 486, L80
Kale R., Venturi T., Cassano R., *et al.* 2015a, A&A, 581, A23
Kale R., Venturi T., Giacintucci S., *et al.* 2015b, A&A, 579, A92
Kale R., Venturi T., Giacintucci S., *et al.* 2013, A&A, 557, A99
Kale R., Wik D. R., Giacintucci S., *et al.* 2017, MNRAS, 472, 940
Kale R., Dwarakanath K. S., Vir Lal D., *et al.* 2016, JoAA, 37, 31
Kang H. 2011, Journal of Korean Astronomical Society, 44, 49
Kang H. 2012, Journal of Korean Astronomical Society, 45, 127
Kang H., Petrosian V., Ryu D., Jones T. W. 2014, ApJ, 788, 142
Kang H., Ryu D. 2011, ApJ, 734, 18
Kang H., Ryu D. 2016, ApJ, 823, 13
Kazantsev A. P. 1968, Soviet Journal of Experimental and Theoretical Physics, 26, 1031
Kempner J. C., Blanton E. L., Clarke T. E., *et al.* 2004, in The Riddle of Cooling Flows in Galaxies and Clusters of galaxies, eds Reiprich T., Kempner J., Soker N., p. 335
Kenyon J. S., Smirnov O. M., Grobler T. L., Perkins S. J. 2018, MNRAS, 478, 2399
Keshet U., Loeb A. 2010, ApJ, 722, 737
Keshet U., Waxman E., Loeb A. 2004, ApJ, 617, 281
Kierdorf M., Beck R., Hoeft M., *et al.* 2017, A&A, 600, A18
Kim K.-T., Kronberg P., Giovannini G., Venturi T. 1989, Nature, 341, 720
Knowles K., Baker A. J., Bond J. R., *et al.* 2019, MNRAS, 486, 1332
Knowles K., Cotton W. D., Rudnick L., *et al.* 2022, A&A, 657, A56
Kolokythas K., Vaddi S., O'Sullivan E., *et al.* 2022, MNRAS, 510, 4191
Kronberg P. P. 1994, Reports on Progress in Physics, 57, 325
Lal D. V. 2020, ApJS, 250, 22
Large M. I., Mathewson D. S., Haslam C. G. T. 1959, Nature, 183, 1663
Li F., Gu Y.-Z., Yuan Q.-R., *et al.* 2019, MNRAS, 484, 3806
Liivamägi L. J., Tempel E., Saar E. 2012, A&A, 539, A80
Locatelli N., Vazza F., Bonafede A., *et al.* 2021, A&A, 652, A80
Locatelli N., Vazza F., Domínguez-Fernández P. 2018, Galaxies, 6, 128
Longair M. S. 2011, High Energy Astrophysics (Cambridge, UK: Cambridge University Press)
Lovisari L., Ettori S., Gaspari M., Giles P. A. 2021, Universe, 7, 139
Lovisari L., Reiprich T. H., Schellenberger G. 2015, A&A, 573, A118
Mahajan S., Haines C. P., Raychaudhury S. 2011, MNRAS, 412, 1098
Mahajan S., Raychaudhury S., Pimbblet K. A. 2012, MNRAS, 427, 1252
Maier A., Iapichino L., Schmidt W., Niemeyer J. C. 2009, ApJ, 707, 40
Malkov M. A., Drury L. O. 2001, Reports on Progress in Physics, 64, 429
Malu S., Datta A., Colafrancesco S., *et al.* 2017, Scientific Reports, 7, 16918
Malu S., Datta A., Sandhu P. 2016, ApSS, 361, 255
Mandal S., Intema H. T., Shimwell T. W., *et al.* 2019, A&A, 622, A22
Mandal S., Intema H. T., van Weeren R. J., *et al.* 2020, A&A, 634, A4
Marinacci F., Vogelsberger M., Pakmor R., *et al.* 2018, MNRAS, 480, 5113
Markevitch M., Vikhlinin A. 2007, Phys. Rep., 443, 1
McKean J., Jackson N., Vegetti S., *et al.* 2015, in Advancing Astrophysics with the Square Kilometre Array (AASKA14), 84
McMullin J. P., Waters B., Schiebel D., Young W., Golap K. 2007, in Astronomical Society of the Pacific Conference Series, Vol. 376, Astronomical Data Analysis Software and Systems XVI, eds Shaw R. A., Hill F., Bell D. J., p. 127
McNamara B. R., Wise M., Nulsen P. E. J., *et al.* 2000, ApJL, 534, L135
Miniati F. 2015, ApJ, 800, 60
Miniati F., Ryu D., Kang H., *et al.* 2000, ApJ, 542, 608
Molnar S. 2016, Frontiers in Astronomy and Space Sciences, 2, 7
Morandi A., Sun M. 2016, MNRAS, 457, 3266
Murgia M., Govoni F., Feretti L., Giovannini G. 2010, A&A, 509, A86
Murgia M., Govoni F., Feretti L., *et al.* 2004, A&A, 424, 429
Murgia M., Parma P., Mack K. H., *et al.* 2011, A&A, 526, A148
Nath B. B., Roychowdhury S. 2002, MNRAS, 333, 145
Nikiel-Wroczyński B., Berger A., Herrera Ruiz N., *et al.* 2019, A&A, 622, A23

Norman M. L., Bryan G. L. 1999, in Lecture Notes in Physics, Berlin Springer Verlag, Vol. 530, The Radio Galaxy Messier 87, eds Röser H.-J., Meisenheimer K., p. 106
Nuza S. E., Gelszinnis J., Hoeft M., Yepes G. 2017, MNRAS, 470, 240
Nuza S. E., Hoeft M., van Weeren R. J., Gottlöber S., Yepes G. 2012, MNRAS, 420, 2006
Offringa A. R., de Bruyn A. G., Biehl M., *et al.* 2010, MNRAS, 405, 155
Offringa A. R., de Bruyn A. G., Zaroubi S. 2012, MNRAS, 422, 563
Offringa A. R., McKinley B., Hurley-Walker, *et al.* 2014, MNRAS, 444, 606
Offringa A. R., Smirnov O. 2017, MNRAS, 471, 301
Ogiya G., Biernacki P., Hahn O., Teyssier R. 2018, arXiv e-prints, 1802.02177
Oozeer N., Rudnick L., Bietenholz M. F., *et al.* 2021, Galaxies, 9, 102
O'Shea B. W., Bryan G., Bordner J., *et al.* 2004, arXiv, astro-ph/0403044. https://doi.org/10.48550/arXiv.astro-ph/0403044
Osinga E., van Weeren R. J., Boxelaar J. M., *et al.* 2021, A&A, 648, A11
O'Sullivan E., Giacintucci S., David L. P., *et al.* 2011a, ApJ, 735, 11
O'Sullivan E., Giacintucci S., David L. P., Vrtilek J. M., Raychaudhury S. 2011b, MNRAS, 411, 1833
Pakmor R., Pfrommer C., Simpson C. M., Springel V. 2016, ApJL, 824, L30
Pandge M. B., Sebastian B., Seth R., Raychaudhury S. 2021, MNRAS, 504, 1644
Pandge M. B., Sonkamble S. S., Parekh V., *et al.* 2019, ApJ, 870, 62
Parekh V., Durret F., Padmanabh P., Pandge M. B. 2017a, MNRAS, 470, 3742
Parekh V., Dwarakanath K. S., Kale R., Intema H. 2017b, MNRAS, 464, 2752
Parekh V., Kincaid R., Hugo B., Ramaila A., Oozeer N. 2021, Galaxies, 9, 90
Parekh V., Laganá T. F., Thorat K., *et al.* 2019, MNRAS, 2668
Parekh V., Thorat K., Kale R., *et al.* 2020, MNRAS, 499, 404
Parekh V., Kincaid R., Thorat K., *et al.* 2022, MNRAS, 509, 3086
Paul S., Gupta P., John R. S., Pubjabi V. 2018, arXiv e-prints, 1803.10764
Paul S., Gupta P., Salunkhe S., *et al.* 2021, MNRAS, 506, 5389
Paul S., Iapichino L., Miniati F., Bagchi J., Mannheim K. 2011, ApJ, 726, 17
Paul S., John R. S., Gupta P., Kumar H. 2017, MNRAS, 471, 2
Paul S., Salunkhe S., Datta A., Intema H. T. 2019, MNRAS, 489, 446
Paul S., Salunkhe S., Sonkamble S., *et al.* 2020, A&A, 633, A59
Pfrommer C., Enßlin T. A. 2004a, A&A, 413, 17
Pfrommer C., Enßlin T. A. 2004b, MNRAS, 352, 76
Pfrommer C., Springel V., Enßlin T. A., Jubelgas M. 2006, MNRAS, 367, 113
Pimbblet K. A., Drinkwater M. J., Hawkrigg M. C. 2004, MNRAS, 354, L61
Pinzke A., Oh S. P., Pfrommer C. 2013, MNRAS, 435, 1061
Pizzo R. F., de Bruyn A. G., Bernardi G., Brentjens M. A. 2011, A&A, 525, A104
Planck Collaboration, Ade P. A. R., Aghanim N., *et al.* 2017, VizieR Online Data Catalog, J/A+A/594/A27
Popesso P., Böhringer H., Brinkmann J., Voges W., York D. G. 2004, A&A, 423, 449
Porter D. H., Jones T. W., Ryu D. 2015, ApJ, 810, 93
Porter S. C., Raychaudhury S. 2005, MNRAS, 364, 1387
Postman M., Geller M. J., Huchra J. P. 1988, AJ, 95, 267
Prasad D., Sharma P., Babul A. 2015, ApJ, 811, 108
Pratt G. W., Arnaud M., Piffaretti R., *et al.* 2010, A&A, 511, A85
Quici B., Hurley-Walker N., Seymour N., *et al.* 2021, PASA, 38, e008
Rahaman M., Raja R., Datta A., *et al.* 2021, MNRAS, 505, 480
Rahaman M., Raja R., Datta A., Burns J. O., Rapetti D. 2022, MNRAS, 515, 2245
Raja R., Rahaman M., Datta A., *et al.* 2021, MNRAS, 500, 2236
Raja R., Rahaman M., Datta A., *et al.* 2020a, MNRAS, 493, L28
Raja R., Rahaman M., Datta A., *et al.* 2020b, ApJ, 889, 128
Rajpurohit K., Vazza F., van Weeren R. J., *et al.* 2021a, A&A, 654, A41
Rajpurohit K., Brunetti G., Bonafede A., *et al.* 2021b, A&A, 646, A135
Rajpurohit K., Hoeft M., Wittor D., *et al.* 2022, A&A, 657, A2
Rau U., Cornwell T. J. 2011, A&A, 532, A71
Raychaudhury S. 1989, Nature, 342, 251
Raychaudhury S., Fabian A. C., Edge A. C., Jones C., Forman W. 1991, MNRAS, 248, 101
Reynolds C. S., McKernan B., Fabian A. C., Stone J. M., Vernaleo J. C. 2005, MNRAS, 357, 242
Richard-Laferrière A., Hlavacek-Larrondo J., Nemmen R. S., *et al.* 2020, MNRAS, 499, 2934
Roettiger K., Stone J. M., Burns J. O. 1999, ApJ, 518, 594
Roncarelli M., Gaspari M., Ettori S., *et al.* 2018, A&A, 618, A39
Roychowdhury S., Ruszkowski M., Nath B. B. 2005, ApJ, 634, 90
Roychowdhury S., Ruszkowski M., Nath B. B., Begelman M. C. 2004, ApJ, 615, 681
Rudnick L., Blundell K. M. 2004, in The Riddle of Cooling Flows in Galaxies and Clusters of galaxies, eds Reiprich T., Kempner J., Soker N., p. 153
Russell H. R., McNamara B. R., Fabian A. C., *et al.* 2019, MNRAS, 490, 3025

Ruszkowski M., Begelman M. C. 2002, ApJ, 581, 223
Rybicki G. B., Lightman A. P. 1986, Radiative Processes in Astrophysics, p. 400, ISBN 0-471-82759-2, Wiley-VCH
Ryu D., Kang H., Cho J. 2010, in Astronomical Society of the Pacific Conference Series, Vol. 429, Numerical Modeling of Space Plasma Flows, Astronum-2009, eds Pogorelov N. V., Audit E., Zank G. P., p. 39
Ryu D., Kang H., Cho J., Das S. 2008, Science, 320, 909
Ryu D., Kang H., Hallman E., Jones T. W. 2003, ApJ, 593, 599
Salunkhe S., Paul S., Krishna G., Sonkamble S., Bhagat S. 2022, A&A, 664, A186
Sarazin C. L. 1986, Rev. Mod. Phys., 58, 1
Sarazin C. L. 2002, in Astrophysics and Space Science Library, Vol. 272, Merging Processes in Galaxy Clusters, eds Feretti L., Gioia I. M., Giovannini G., p. 1
Savini F., Bonafede A., Brüggen M., *et al.* 2018, MNRAS, 478, 2234
Savini F., Bonafede A., Brüggen M., *et al.* 2019, A&A, 622, A24
Saxton C. J., Sutherland R. S., Bicknell G. V. 2001, ApJ, 563, 103
Schekochihin A. A., Cowley S. C., Taylor S. F., Maron J. L., McWilliams J. C. 2004, ApJ, 612, 276
Schellenberger G., Vrtilek J. M., David L., *et al.* 2017, ApJ, 845, 84
Schellenberger G., Giacintucci S., Lovisari L., *et al.* 2022, ApJ, 925, 91
Schlickeiser R., Sievers A., Thiemann H. 1987, A&A, 182, 21
Schmidt W., Federrath C., Hupp M., Kern S., Niemeyer J. C. 2009, A&A, 494, 127
Schulz R., Dijkema T. J., Molenaar G. 2020, Apercal: Pipeline for the Westerbork Synthesis Radio Telescope Apertif upgrade ascl:2002.010
Seta A., Bushby P. J., Shukurov A., Wood T. S. 2020, Physical Review Fluids, 5, 043702
Seta A., Federrath C. 2021, Physical Review Fluids, 6, 103701
Seth R., Raychaudhury S. 2020, MNRAS, 497, 466
Shimwell T. W., Tasse C., Hardcastle M. J., *et al.* 2019, A&A, 622, A1
Sweijen F., van Weeren R. J., Röttgering H. J. A., *et al.* 2022, Nature Astronomy, 6, 350
Shimwell T. W., Hardcastle M. J., Tasse C., *et al.* 2022, A&A, 659, A1
Sijbring L. G. 1993, PhD thesis, University of Groningen, The Netherlands
Silpa S., Kharb P., Harrison C. M., *et al.* 2021, MNRAS, 507, 991
Skillman S. W., Hallman E. J., O'Shea B. W., *et al.* 2011, ApJ, 735, 96
Skillman S. W., O'Shea B. W., Hallman E. J., Burns J. O., Norman M. L. 2008, ApJ, 689, 1063
Šlaus B., Smolčić V., Novak M., *et al.* 2020, A&A, 638, A46
Slee O. B., Roy A. L., Murgia M., Andernach H., Ehle M. 2001, AJ, 122, 1172
Sommer M. W., Basu K. 2014, MNRAS, 437, 2163
Springel V., Frenk C. S., White S. D. M. 2006, Nature, 440, 1137
Stroe A., Harwood J. J., Hardcastle M. J., Röttgering H. J. A. 2014a, MNRAS, 445, 1213
Stroe A., Rumsey C., Harwood J. J., *et al.* 2014b, MNRAS, 441, L41
Stroe A., Shimwell T., Rumsey C., *et al.* 2016, MNRAS, 455, 2402
Su Y., Nulsen P. E. J., Kraft R. P., *et al.* 2017, ApJ, 847, 94
Subramanian K., Shukurov A., Haugen N. E. L. 2006, MNRAS, 366, 1437
Sur S. 2019, MNRAS, 488, 3439
Sur S., Basu A., Subramanian K. 2021, MNRAS, 501, 3332
Sur S., Bhat P., Subramanian K. 2018, MNRAS, 475, L72
Swarup G., Ananthakrishnan S., Kapahi V. K., *et al.* 1991, Current Science, 60, 95
Tarenghi M., Tifft W. G., Chincarini G., Rood H. J., Thompson L. A. 1979, ApJ, 234, 793
Tasse C. 2014, arXiv e-prints, 1410.8706
Tasse C., Hugo B., Mirmont M., *et al.* 2018, A&A, 611, A87
Tempel E., Stoica R. S., Martínez V. J., *et al.* 2014, MNRAS, 438, 3465
Tripp T. M., Savage B. D., Jenkins E. B. 2000, ApJL, 534, L1
Tully R. B., Courtois H., Hoffman Y., Pomarède D. 2014, Nature, 513, 71
Vacca V., Murgia M., Govoni F., *et al.* 2018, MNRAS, 479, 776
Valdarnini R. 2011, A&A, 526, A158
van de Weygaert R., Bond J. R. 2008, in A Pan-Chromatic View of Clusters of Galaxies and the Large-Scale Structure, eds Plionis M., López-Cruz O., Hughes D., Vol. 740, p. 335
van Haarlem M. P., Wise M. W., Gunst A., *et al.* 2013, A&A, 556, A2
van Weeren R. J., de Gasperin F., Akamatsu H., *et al.* 2019, SSR, 215, 16
van Weeren R. J., Röttgering H. J. A., Brüggen M., Hoeft M. 2010, Science, 330, 347
van Weeren R. J., Röttgering H. J. A., Bagchi J., *et al.* 2009, A&A, 506, 1083
van Weeren R. J., Intema H. T., Lal D. V., *et al.* 2014, ApJL, 786, L17
van Weeren R. J., Brunetti G., Brüggen M., *et al.* 2016, ApJ, 818, 204
van Weeren R. J., Shimwell T. W., Botteon A., *et al.* 2021, A&A, 651, A115
Vazza F. 2010, in Galaxy Clusters: Observations, Physics and Cosmology, 24
Vazza F., Brüggen M., Gheller C., Brunetti G. 2012a, MNRAS, 421, 3375
Vazza F., Roediger E., Brüggen M. 2012b, A&A, 544, A103
Vazza F., Brunetti G., Gheller C. 2009a, MNRAS, 395, 1333
Vazza F., Brunetti G., Kritsuk A., *et al.* 2009b, A&A, 504, 33

Vazza F., Brunetti G., Gheller C., Brunino R., Brüggen M. 2011, A&A, 529, A17
Vazza F., Brunetti G., Brüggen M., Bonafede A. 2018, MNRAS, 474, 1672
Vazza F., Ferrari C., Brüggen M., *et al.* 2015, A&A, 580, A119
Vazza F., Tormen G., Cassano R., Brunetti G., Dolag K. 2006, MNRAS, 369, L14
Vazza F., Jones T. W., Brüggen M., *et al.* 2017, MNRAS, 464, 210
Vazza F., Wittor D., Brunetti G., Brüggen M. 2021a, A&A, 653, A23
Vazza F., Locatelli N., Rajpurohit K., *et al.* 2021b, Galaxies, 9, 109
Venturi T., Giacintucci S., Brunetti G., *et al.* 2007, A&A, 463, 937
Venturi T., Giacintucci S., Dallacasa D., *et al.* 2008, A&A, 484, 327
Venturi T., Giacintucci S., Dallacasa D., *et al.* 2013, A&A, 551, A24
Venturi T., Rossetti M., Brunetti G., *et al.* 2017, A&A, 603, A125
Venturi T., Giacintucci S., Merluzzi P., *et al.* 2022, A&A, 660, A81
Vernstrom T., Gaensler B. M., Brown S., Lenc E., Norris R. P. 2017, MNRAS, 467, 4914
Vikhlinin A., Kravtsov A., Forman W., *et al.* 2006, ApJ, 640, 691
Völk H. J., Atoyan A. M. 1999, Astroparticle Physics, 11, 73
Wiener J., Pfrommer C., Peng Oh S. 2017, MNRAS, 467, 906
Wilber A., Brüggen M., Bonafede A., *et al.* 2019, A&A, 622, A25
Wilber A. G., Johnston-Hollitt M., Duchesne S. W., *et al.* 2020, PASA, 37, e040
Wilcots E. 2004, Nature, 48, 1281
Willson M. A. G. 1970, MNRAS, 151, 1
Wittor D., Ettori S., Vazza F., *et al.* 2021a, MNRAS, 506, 396
Wittor D., Hoeft M., Brüggen M. 2021b, Galaxies, 9, 111. https://doi.org/10.3390/galaxies9040111
Wittor D., Hoeft M., Vazza F., Brüggen M., Domínguez-Fernández P. 2019, MNRAS, 490, 3987
Xu H., Govoni F., Murgia M., *et al.* 2012, ApJ, 759, 40
Yan H., Lazarian A. 2002, PRL, 89, 281102
Yan H., Lazarian A. 2004, ApJ, 614, 757
Yan H., Lazarian A., Petrosian V. 2008, ApJ, 684, 1461
Zeldovich Y. B., Ruzmaikin A. A., Sokoloff D. D. 1990, The almighty chance https://doi.org/10.1142/0862